Chapter 6

Model Neurons

6.1 Levels of Neuron Modeling

A great deal is known about the biophysical mechanisms responsible for generating neuronal activity, and the mathematical descriptions of these mechanisms presented in chapter 5 provide a basis for constructing neuron models. These models range from highly detailed descriptions involving thousands of coupled differential equations to greatly simplified caricatures useful for large network modeling. In this chapter, we present a number of different approaches to modeling neuronal activity that vary considerably in their level of detail. Choosing the most appropriate modeling level for a given research problem requires a careful assessment of the experimental information available and a clear understanding of the research goals. Oversimplified models can, of course, give misleading results, but excessively detailed models can obscure interesting results beneath inessential and unconstrained complexity.

In modeling neurons, we must deal with two basic types of complexity: elaborate morphologies and conductances with rich dynamics. As discussed in chapter 5, the membrane potential of a neuron with a complex morphology depends on both time and spatial position, $V(x,t)$. The cable equation that determines $V(x,t)$ was discussed in chapter 5, but the analytic methods presented there can only be applied when the membrane conductances are voltage-independent. When the complexities of real membrane conductances are included, the membrane potential must be computed numerically. This is done by breaking up the neuron into separate regions or compartments and approximating the continuous membrane potential $V(x,t)$ by a discrete set of values representing the potentials within the different compartments. This assumes that each compartment is small enough so that there is negligible variation in the membrane potential across it. The precision of such a multi-compartmental description depends on the number of compartments used and on the compactness of the neuron being modeled. Figure 6.1 shows a schematic diagram of a cortical pyramidal neuron, along with a series of compartmental approximations of its structure. The number of compartments used can range from thousands in some models to one for the description at the extreme right of figure 6.1. In single compartment models, the entire neuron is described by a single membrane potential and all position-dependent variations are ignored. This is only valid if the neuron is fairly compact, or if the behavior being studied is not strongly affected by potential differences between different parts of the neuron.

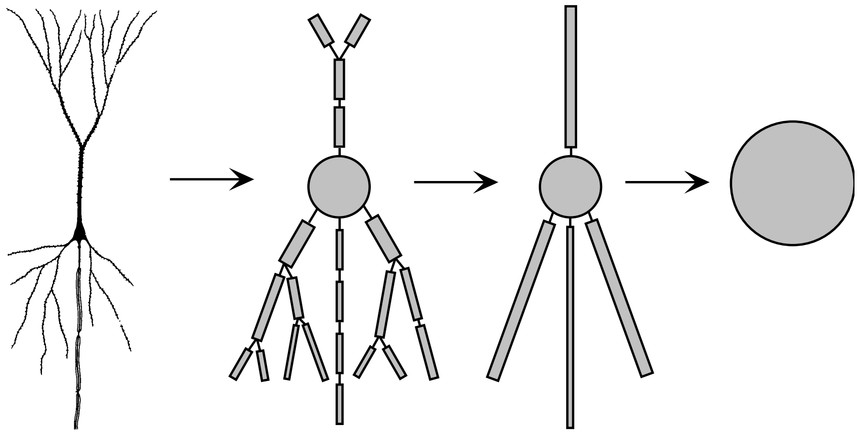

Figure 6.1: A sequence of approximations for the structure of a neuron. The neuron is represented by a variable number of discrete compartments each representing a region that is described by a single membrane potential. The connectors between compartments represent resistive couplings. The simplest description is the single-compartment model furthest to the right. (Neuron diagram from Haberly, 1990)

One of the most problematic features in neuron modeling is the tremendous dynamic range of neuronal membrane and synaptic conductances. The fastest conductances in a typical neuron, those responsible for initiating the action potential, activate in less than a millisecond. Slower conductances have time constants in the range of hundreds of milliseconds. Various modulatory processes can affect conductances over times varying from minutes to hours, or even longer. Thus, the complete dynamic range extends over several orders of magnitude. In most models, this is collapsed to a much smaller range to keep the time needed to numerically integrate the equations of the model reasonable.

The ionic conductances that give a neuron its electrical properties are time-dependent nonlinear functions of voltage and other factors. Models that treat these aspects of ionic conductances are known as conductance-based models. The basic formalism developed by Hodgkin and Huxley to describe the $\mathtt{Na}^+$ and $\mathtt{K}^+$ conductances responsible for generating action potentials (discussed in chapter 5) is used to represent most of the additional conductances encountered in neuron modeling. Neuron models based on these mathematical descriptions of membrane conductances can reproduce the rich and complex dynamics of real neurons quite accurately. In this chapter, we discuss both single- and multi-compartment conductance-based models.

When large networks of neurons are modeled, simplified descriptions of the individual neurons are often employed. This speeds up simulations of large networks, simplifies the analysis of their activity patterns, and avoids the problem of setting large numbers of free parameters that are not constrained by experimental measurements. We discuss a particularly useful simplified model of a spiking neuron, the integrate-and-fire model, quite extensively. We conclude the chapter by analyzing a complementary approach, neuron models based on firing-rate descriptions that provide the basis for the network models discussed in chapters 7 and 8.

6.2 Single-Compartment Models

In any neuron model, the rate of change of the membrane potential within a portion of the neuron is determined by the total current flowing into that region (see chapter 5). For a single-compartment model, the region in question is the entire neuron, and the relevant currents are those arising from all the membrane and synaptic conductances of the cell. The sum of all these currents is set equal to the total capacitance of the neuron times the rate of change of the membrane potential. Because membrane and synaptic currents are usually expressed as currents per unit area of membrane, it is more convenient to re-express this relation so that the total current per unit area of membrane is equal to the capacitance per unit area, c_{m} (usually taken to be 10 nF/mm^2), times the rate of change of the membrane potential. We also include a current I_{e} coming from an external electrode inserted into the neuron. Electrode currents are not typically expressed as current per unit area of membrane, so to match the other currents we must divide the injected current by the total surface area of the neuron, A. Putting all this together, the basic equation for all single-compartment models is

$$c_{\mathrm{m}} \frac{dV}{dt} = -i_{\mathrm{m}} - i_{\mathrm{s}} + \frac{I_{\mathrm{e}}}{A} \tag{6.1}$$

where i_{m} is the total current per unit area from all membrane conductances, and i_{s} is the total current per unit area due to synaptic conductances. By convention, current that enters the neuron through an electrode is defined as positive-inward, whereas membrane and synaptic currents are defined as positive-outward. This explains the different signs for the currents in equation 6.1. Single-compartment neuron models all use equation 6.1, but they differ in the degree of detail with which the dynamics of the membrane and synaptic conductances are treated.

Conductance-Based Models

The formalism developed by Hodgkin and Huxley (1952) (see chapter 5) to describe the fast Na^+ and delayed-rectifier K^+ conductances in the squid giant axon has, by now, been applied successfully to dozens of conductances in a wide variety of preparations. On the basis of these conductance descriptions, it is possible to construct complex and reasonably accurate models of neurons displaying a wide range of activity patterns. Efficient numerical methods make it possible to run computer simulations that reproduce the activity of real neurons rapidly and with a high degree of accuracy.

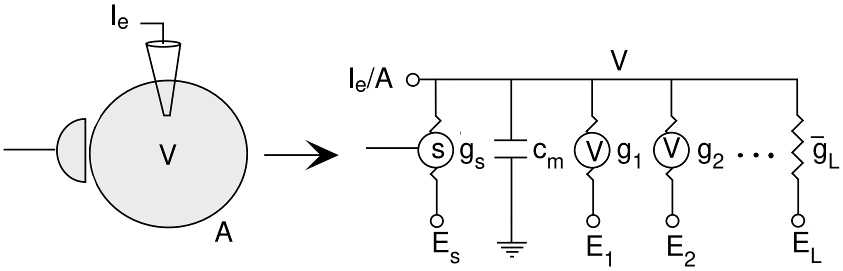

Figure 6.2: The equivalent circuit for a one-compartment conductance-based neuron model. The neuron is modeled, at left, as a single compartment with a synapse and a current injecting electrode. At right is the equivalent circuit. The ellipses stand for an unspecified number of membrane conductances. The circled s indicates a synaptic conductance that depends on the activity of a presynaptic neuron. A single synaptic conductance is indicated, but, in general, there may be several different types. The circled V indicates a voltage-dependent conductance. I_e is the current passing through the electrode, and A is the surface area of the neuron.

The membrane potential for a single-compartment conductance-based neuron model is determined by integrating equation 6.1 (see Appendix A). The membrane and synaptic currents per unit area are written in terms of the membrane and synaptic conductances, open probabilities, or gating variables (see chapter 5) as

$$i_\mathrm{m} + i_\mathrm{s} = \sum_i g_i(V - E_i) = \sum_i \overline{g}_i P_i(V - E_i) = \sum_i \overline{g}_i m_i^{p_i} h_i^{q_i}(V - E_i) \tag{6.2}$$

where the parameters $\overline{g}_i$ are fixed maximal conductances (the conductance per unit area when $P = 1$). Note that we have included both membrane and synaptic conductances in this sum, because both are describe similarly in terms of gating variables and reversal potentials. One of the membrane conductances is the leakage conductance with $P = 1$. Figure 6.2 shows the equivalent circuit for a generic one-compartment model with a number of different conductances.

The dynamic variables of a single-compartment conductance-based model are the membrane potential, V, and the activation and inactivation gating variables for the different conductances. We have distinguished the different gating variables in equation 6.2 by the subscript i, but often they are distinguished instead by using letters other than m and h. For example, the activation variable for the delayed-rectifier K^+ conductance is conventionally denoted by n (see chapter 5). As discussed in chapter 5, all of the gating variables (whether denoted by m, h, or some other letter) are determined by equations of the form

$$\tau_z(V)\frac{dz}{dt} = z_\infty(V) - z \tag{6.3}$$

where we have used the letter z to denote a generic gating variable. The functions $\tau_z(V)$ and $z_\infty(V)$ are determined from experimental data. For some conductances, these are written in terms of the open and closing rates $\alpha_z(V)$ and $\beta_z(V)$ (see chapter 5) as

$$\tau_z(V) = \frac{1}{\alpha_z(V)+\beta_z(V)} \quad \text{and} \quad z_\infty(V) = \frac{\alpha_z(V)}{\alpha_z(V)+\beta_z(V)}\,. \tag{6.4}$$

We have written $\tau_z(V)$ and $z_\infty(V)$ as functions of the membrane potential, but for Ca^{2+}-dependent currents they also depend on the internal Ca^{2+} concentration. For synaptic conductances, the gating variables depend on the concentration of transmitter in the synaptic cleft, but they are often written directly in terms of the presynaptic membrane potential or the times when presynaptic action potentials occur (see chapter 5). A method for numerically integrating the equations for the gating variables of a conductance-based model is described in Appendix B.

In the following sections, some basic features of conductance-based models are presented in a sequence of examples of increasing complexity. We do this to illustrate the effects of various conductances and combinations of conductances on neuronal activity.

The Connor-Stevens Model

The Hodgkin-Huxley model of action potential generation, discussed in chapter 5, was developed on the basis of data from the giant axon of the squid, and we present a multi-compartment simulation of action potential propagation using this model in a later section. The Connor-Stevens model provides an alternative description of action potential generation. Like the Hodgkin-Huxley model, it contains fast Na^+, delayed-rectifier K^+, and leakage conductances. The fast $Na^+$and delayed-rectifier K^+ conductances have somewhat different properties from those of the Hodgkin-Huxley model, in particular faster kinetics, so the action potentials are briefer. In addition, the Connor-Stevens model contains an extra K^+ conductance, called the A-current, that is transient.

The membrane current in the Connor-Stevens model is

$$i_m = \overline{g}_L(V - E_L) + \overline{g}_{Na}m^3h(V - E_{Na}) + \overline{g}_K n^4(V - E_K) + \overline{g}_A a^3 b(V - E_A) \tag{6.5}$$

where $\overline{g}_{\mathrm{L}} = 3\,\mu\mathrm{S/mm}^2$ and E_{L} = -17 mV are the maximal conductance and reversal potential for the leak conductance, and $\overline{g}_{\mathrm{K}} = 200\,\mu\mathrm{S/mm}^2$, $\overline{g}_{\mathrm{Na}} = 1200\,\mu\mathrm{S/mm}^2$, $\overline{g}_{\mathrm{A}} = 477\,\mu\mathrm{S/mm}^2$, E_{K} = -72 mV, E_{A} = -75 mV and E_{Na} = 55 mV are similar parameters for the active conductances. The gating variables, m, h, n, a, and b, are determined by equations of the form 6.3. The α and β functions for the Na$^+$ and delayed-rectifier K$^+$ conductances are (with α and β in units of 1/ms and V in units of mV)

$$\begin{aligned}
\alpha_m &= \frac{0.38(V+29.7)}{1-\exp[-0.1(V+29.7)]} & \beta_m &= 15.2\exp[-0.0556(V+54.7)] \\
\alpha_h &= 0.266\exp[-0.05(V+48)] & \beta_h &= 3.8/(1+\exp[-0.1(V+18)]) \\
\alpha_n &= \frac{0.02(V+45.7)}{1-\exp[-.1(V+45.7)]} & \beta_n &= 0.25\exp[-0.0125(V+55.7)]\,. \qquad (6.6)
\end{aligned}$$

The A-current is described directly in terms of the asymptotic values and τ functions for its gating variables (with τ_a and τ_b in units of ms and V in units of mV),

$$a_\infty = \left[\frac{0.0761\exp[.0314(V+94.22)]}{1+\exp[0.0346(V+1.17)]}\right]^{1/3} \qquad (6.7)$$

$$\tau_a = 0.3632 + 1.158/(1+\exp[0.0497(V+55.96)]) \qquad (6.8)$$

$$b_\infty = \left[\frac{1}{1+\exp[0.0688(V+53.3)]}\right]^4 \qquad (6.9)$$

and

$$\tau_b = 1.24 + 2.678/(1+\exp[0.0624(V+50)])\,. \qquad (6.10)$$

Figure 6.3 illustrates action potential generation in the Connor-Stevens model. In the absence of injected external current or synaptic input, the membrane potential of the model remains constant at a resting value of -68 mV. With constant positive current injection ($I_{\mathrm{e}} > 0$), the model neuron depolarizes until a threshold current is reached and the model generates action potentials. Figure 6.3A shows how the firing rate of the model depends on the magnitude of the injected current relative to the threshold value. The firing rate rises continuously from zero and then increases roughly linearly for currents over the range shown. For larger currents, the firing rate increases more slowly and ultimately saturates. Figure 6.3B shows an example of action potential generation due to constant current injection.

The fast Na$^+$ and delayed-rectifier K$^+$ conductances in the Connor-Stevens model generate action potentials in the same way they do in the Hodgkin-Huxley model (see chapter 5). What is the role of the addition A-current? Figure 6.3C shows the firing rate as a function of injected current for the

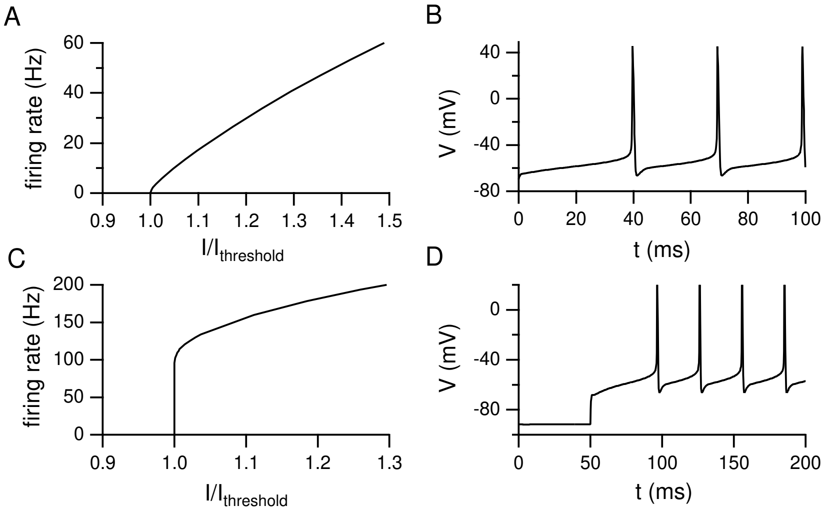

Figure 6.3: Firing of action potentials in the Connor-Stevens model. A) Firing rate as a function of injected current. The firing rate rises continuously from zero as the current increases beyond the threshold value. B) An example of action potentials generated by constant current injection. C) Firing rate as a function of injected current when the A-current is turned off. The firing rate now rises discontinuously from zero as the current increases beyond the threshold value. D) Delayed firing due to hyperpolarization. The neuron was held hyperpolarized for a prolonged period by injection of negative current. At $t = 50$ ms, the negative injected current was switched to a positive value. The A-current delays the occurance of the first action potential.

Connor-Stevens model with the maximal conductance of the A-current set to zero. The leakage conductance and reversal potential have been adjusted to keep the same resting potential and input resistance as in the original model. The firing rate is clearly much faster with the A-current turned off. In addition, the transition from no firing for currents less than the threshold value to firing with suprathreshold currents is different when the A-current is eliminated. Without the A-current, the firing rate jumps discontinuously to a nonzero value rather than rising continuously. Neurons with firing rates that rise continuously from zero as a function of injected current are called type I, and those with discontinuous jumps in their firing rates at threshold are called type II. An A-current is not required to produce a type I response but, as figures 6.3A and 6.3C show, it plays this role in the Connor-Stevens model. The Hodgkin-Huxley model produces a type II response.

Another effect of the A-current is illustrated in figure 6.3D. Here the model neuron was held hyperpolarized by negative current injection for an extended period of time, and then the current was switched to a positive value. While the neuron is hyperpolarized, the A-current deinactivates; that is, the variable b increases toward one. When the injected current switches sign and the neuron depolarizes, the A-current first activates and then inactivates. This delayes the first spike following the change in the injected current.

Postinhibitory Rebound and Bursting

The range of responses exhibited by the Connor-Stevens model neuron can be extended by including a transient Ca^{2+} conductance. The conductance we use was modeled by Huguenard and McCormick (1992) on the basis of data from thalamic relay cells. The membrane current due to the transient Ca^{2+} conductance is expressed as

$$i_{\mathrm{CaT}} = \overline{g}_{\mathrm{CaT}} M^2 H (V - E_{\mathrm{Ca}}) \tag{6.11}$$

with, for the example given here, $\overline{g}_{\mathrm{CaT}} = 13\ \mu\mathrm{S/mm}^2$ and $E_{\mathrm{Ca}} = 120$ mV. The gating variables for the transient Ca^{2+} conductance are determined by (with τ_M and τ_H in ms and V in mV)

$$M_\infty = \frac{1}{1 + \exp\left(-(V + 57)/6.2\right)} \tag{6.12}$$

$$H_\infty = \frac{1}{1 + \exp\left((V + 81)/4\right)} \tag{6.13}$$

$$\tau_M = 0.612 + \left(\exp\left(-(V + 132)/16.7\right) + \exp\left((V + 16.8)/18.2\right)\right)^{-1} \tag{6.14}$$

and

$$\tau_H = \begin{cases} \exp\left((V + 467)/66.6\right) & \text{if } V < -80 \text{ mV} \\ 28 + \exp\left(-(V + 22)/10.5\right) & \text{if } V \geq -80 \text{ mV}\,. \end{cases} \tag{6.15}$$

A transient Ca^{2+} conductances acts, in many ways, like a slower version of the transient Na^{+} conductance that generates action potentials. Instead of producing an action potential, the transient Ca^{2+} conductance generates a slower transient depolarization sometimes called a Ca^{2+} spike. This transient depolarization causes the neuron to fire a burst of action potentials, which are Na^{+} spikes riding on the slower Ca^{2+} spike. Figure 6.4 shows such a burst and illustrates one way to produce it. In this example, the model neuron was hyperpolarized for an extended period and then released from hyperpolarization by setting the current to zero. During the prolonged hyperpolarization, the transient Ca^{2+} conductance deinactivated. When the injected current was set to zero, the resulting depolarization activated the transient Ca^{2+} conductance and generated a burst of action potentials. The burst in figure 6.4 is delayed due to the presence of the A-current in the original Connor-Stevens model, and it terminates when the Ca^{2+} conductances inactivates. Generation of action potentials

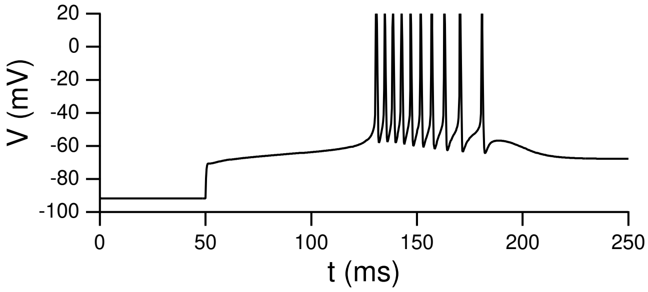

Figure 6.4: A burst of action potentials due to rebound from hyperpolarization. The model neuron was held hyperpolarized for an extended period (until the conductances came to equilibrium) by injection of constant negative external current. At $t = 50$ ms, the injected current was set to zero and a burst of $\mathtt{Na}^+$ spikes was generated due to an underlying $\mathtt{Ca}^{2+}$ spike.

in response to release from hyperpolarization is called postinhibitory rebound because, in a natural setting, the hyperpolarization would be caused by inhibitory synaptic input, not by current injection.

The transient $\mathtt{Ca}^{2+}$ current is an important component of models of thalamic relay neurons. These neurons exhibit different firing patterns in sleep and wakeful states. Action potentials tend to appear in bursts during sleep. Figure 6.5 shows an example of three states of activity of a model thalamic relay cell due to Wang (1994) that has, in addition to fast $\mathtt{Na}^+$, delayed-rectifier $\mathtt{K}^+$, and transient $\mathtt{Ca}^{2+}$ conductances, a hyperpolarization activated mixed-cation conductance and a persistent $\mathtt{Na}^+$ conductance. The model is silent or fires action potentials in a regular pattern or in bursts depending on the level of current injection. In particular, injection of small amounts of negative current leads to bursting. This occurs because the hyperpolarization due to the current injection deinactivates the transient $\mathtt{Ca}^{2+}$ current and activates the hyperpolarization activated current.

Neurons can fire action potentials either at a steady rate or in bursts even in the absence of current injection or synaptic input. Periodic bursting is a common feature of neurons in central patterns generators, which are neural circuits that produce periodic patterns of activity to drive rhythmic motor behaviors such as walking, running, or chewing. To illustrate periodic bursting, we consider a model constructed to match the activity of neurons in the crustacean stomatogastric ganglion (STG), a neuronal circuit that controls chewing and digestive rhythms in the foregut of lobsters and crabs (this is a variant of the model of Turrigiano, LeMasson, and Marder, 1995 due to Z. Liu and M. Goldman). The model contains fast $\mathtt{Na}^+$, delayed-rectifier $\mathtt{K}^+$, A-type $\mathtt{K}^+$, and transient $\mathtt{Ca}^{2+}$ conductances similar to those discussed above, although the formulae and parameters used are somewhat different. In addition, the model has a $\mathtt{Ca}^{2+}$-dependent $\mathtt{K}^+$ conductance. Due to the complexity of the model,

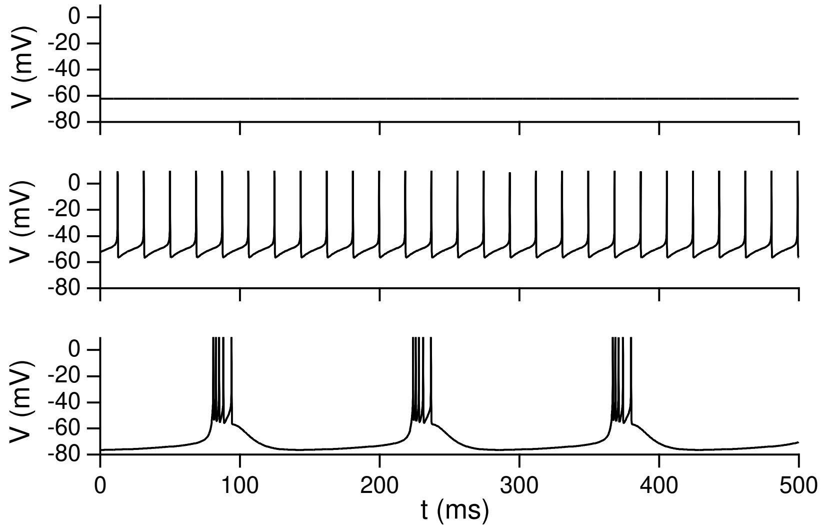

Figure 6.5: Three activity modes of a model thalamic neuron. Upper panel: with no injected current the model is silent. Middle panel: when a positive current is injected into the model neuron, it fires action potentials in a regular periodic pattern. Lower panel: when negative current is injected into the model neuron, it fires action potentials in periodic bursts. (Adapted from Wang, 1994)

we do not provide complete descriptions of its conductances except for the $\texttt{Ca}^{2+}$-dependent $\texttt{K}^+$ conductance, a type of conductance we have not yet discussed. This conductance plays a particularly significant role in the model.

The $\texttt{Ca}^{2+}$-dependent $\texttt{K}^+$ current is given by

$$i_{\text{KCa}} = \overline{g}_{\text{KCa}} c^4 (V - E_{\text{K}}) \tag{6.16}$$

where (with V in mV)

$$c_\infty = \left(\frac{[\texttt{Ca}^{2+}]}{[\texttt{Ca}^{2+}] + 3\mu\text{M}}\right) \frac{1}{1 + \exp(-(V + 28.3)/12.6)} \tag{6.17}$$

and (with τ_c in ms and V in mV)

$$\tau_c = 90.3 - \frac{75.1}{1 + \exp(-(V + 46)/22.7)} \,. \tag{6.18}$$

Note that c_∞ depends on both the membrane potential and the intracellular $\texttt{Ca}^{2+}$ concentration, $[\texttt{Ca}^{2+}]$.

The intracellular $\texttt{Ca}^{2+}$ concentration is computed in this model using a greatly simplified description in which rises in intracellular $\texttt{Ca}^{2+}$ are caused by influx through membrane $\texttt{Ca}^{2+}$ channels, and $\texttt{Ca}^{2+}$ removal is described by an exponential process. The resulting equation for the intracellular Ca^{2+} concentration, $[\mathrm{Ca}^{2+}]$, is

$$\frac{d[\mathrm{Ca}^{2+}]}{dt} = -\gamma i_{\mathrm{Ca}} - \frac{[\mathrm{Ca}^{2+}]}{\tau_{\mathrm{Ca}}} . \tag{6.19}$$

Here i_{Ca} is the total Ca^{2+} current per unit area of membrane, τ_{Ca} is the time constant determining the Ca^{2+} uptake rate, and

$$\gamma = \left(\frac{A}{\mathrm{Vol}F}\right)\left(\frac{10^6\ \mathrm{mm}^3}{\mathrm{liter}}\right) \tag{6.20}$$

where A is the total surface area of the cell, Vol is its total volume, and F is the Faraday constant. The factor γ converts the Ca^{2+} current, which is measured as a current per unit area, into a volume flux of Ca^{2+} measured in mol units.

Figure 6.6 shows the model firing action potentials in bursts. As in the models of figures 6.4 and 6.5, the bursts are transient Ca^{2+} spikes with action potentials riding on top of them. The Ca^{2+} current during these bursts causes a dramatic increase in the intracellular Ca^{2+} concentration. This activates the Ca^{2+}-dependent K^{+} current which, along with the inactivation of the Ca^{2+} current, terminates the burst. The interburst interval is determined primarily by the time it takes for the intracellular Ca^{2+} concentration to return to a low value, which deactivates the Ca^{2+}-dependent K^{+} current and allows another burst to be generated. Although figure 6.6 shows that the conductance of the Ca^{2+}-dependent K^{+} current reaches a low value immediately after each burst, this initial dip is too early for another burst to be generated at that point in the cycle.

Activity-Dependent Conductances

Conductance-based neuron modeling is an area of computational neuroscience where experimental data and mathematical descriptions can be matched to a high degree of accuracy. Nevertheless, there are significant problems associated with conductance-based neuron models that can make them frustrating to construct and difficult to interpret. The most problematic feature is the large number of free parameters in these model. For example, the maximal conductances parameters are typically set by hand until the activity of the model neuron matches that of its biological counterpart. Most models are quite sensitive to the precise values of the maximal conductances, and experimental measurements cannot specify them accurately enough to avoid this fine-tuning procedure. The dynamics of these models is typically complex, and matching a given type of activity can be a frustrating exercise in parameter fitting. Given the difficulty that modelers have in finding the right parameters to generate a particular pattern of activity, it is natural to ask how neurons are able to develop and maintain the conductances they need to function properly.

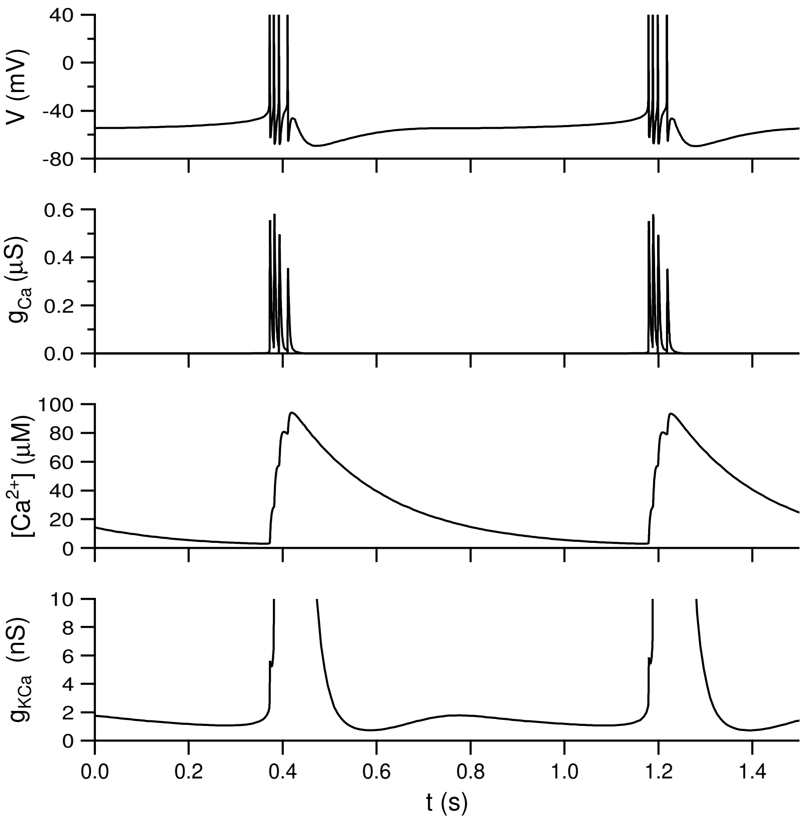

Figure 6.6: Periodic bursting in a model of a crustacean stomatogastric ganglion neuron. From the top, the panels show the membrane potential, the Ca^{2+} conductance, the intracellular Ca^{2+} concentration, and the Ca^{2+}-dependent K^{+} conductance. The Ca^{2+}-dependent K^{+} conductance is shown at an expanded scale so the reduction of the conductance due to the falling intracellular Ca^{2+} concentration during the interburst intervals can be seen. In this example, $\tau_{\mathrm{Ca}} = 200$ ms. (Simulation by M. Goldman.)

Ion channels in neurons are continually being synthesized, transported to various parts of the cell and inserted into the membrane while old channels are removed and disassembled. While in the membrane, channels are subject to a variety of modulatory influences. It seems likely that the electrical activity of a neuron plays a role in regulating all of these processes, so that the neuron can actively maintain the ion channels it needs to function properly. Thinking along these lines, LeMasson, Marder and Abbott (1993) proposed a model in which the maximal conductances of membrane currents are regulated by the activity of the neuron through the intracellular Ca^{2+} concentration. In this model, the maximal conductances are not fixed parameters as in conventional models, but instead can change over time governed by the intracellular Ca^{2+} level, $[\mathrm{Ca}^{2+}]$. Because Ca^{2+} enters a

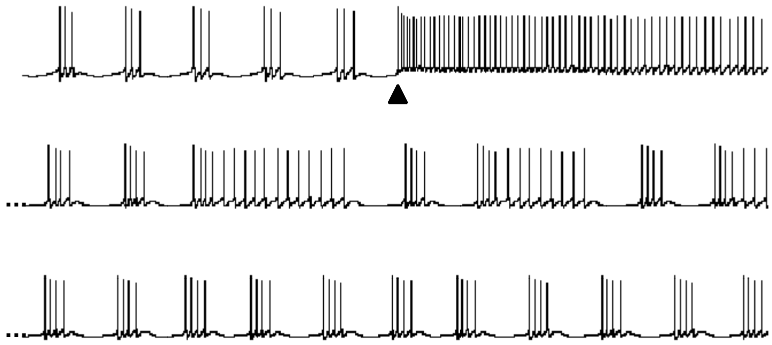

Figure 6.7: The effect of changing E_K on a model neuron with activity-dependent conductances. Initially the model was in a bursting state. At the time indicated by the triangle, a rise in extracellular K^+ was simulated by changing the value of E_K. This caused the neuron to switch its firing pattern. After a readjustment period, bursting was restored. (Adapted from LeMasson *et al*, 1993)

neuron through voltage-dependent channels, the intracellular Ca^{2+} concentration is a good indicator of electrical activity. Thus, the regulation of maximal conductances by $[Ca^{2+}]$ provides a feedback loop linking the electrical activity of a neuron to the conductances that produce it. Bell (1992) and Stemmler and Koch (1999) have proposed related models and provide information-theoretic interpretations of activity-dependent conductance regulation.

Neuron models with activity-dependent regulation of conductances can self-assemble, adjusting their maximal conductances until a fixed pattern of activity has been established. Once assembled, these models are extremely stable and robust. Figure 6.7 shows a model that is initially in a stable configuration in which it fired action potentials in bursts. At the time indicated by the triangle in figure 6.7, an increase in the amount of extracellular K^+ was simulated by changing the K^+ reversal potential E_K. This caused the neuron to shift into a fast firing mode, rather than bursting. Due to the increased activity, the intracellular Ca^{2+} concentration increased and the maximal conductances were modified by the model. The result of this modification was a return to a bursting mode of activity as seen in the bottom trace of figure 6.7. Thus, models with activity-dependent conductances are far more robust than those with fixed conductances, and they may crudely approximate the types of adaptations real neurons are capable of making in order to develop and maintain their electrical properties.

Integrate-and-Fire Models

When the membrane potential of a neuron reaches a threshold value, normally between -55 and -50 mV, it will typically fire an action potential. The action potential follows a rapid stereotyped trajectory, and then the membrane potential returns to a value hyperpolarized relative to the action potential threshold. As we have seen, the mechanisms by which voltage-dependent K^+ and Na^+ conductances produce action potentials are well-understood and can be modeled quite accurately. On the other hand, neuron models can be simplified, and simulations can be accelerated dramatically, if the biophysical mechanisms responsible for the action potentials are not explicitly included in the model. This is the approach used in integrate-and-fire models. Integrate-and-fire models generate action potentials by imposing a fixed rule rather than by computing the membrane potential trajectory on the basis of modeled conductances. These models simply stipulate that an action potential occurs whenever the membrane potential of the model neuron reaches a threshold value V_{th}. After that action potential, the potential is reset to a value V_{reset}.

The basic integrate-and-fire model was proposed by Lapicque in 1907, long before the mechanisms that generate the action potential were understood. Despite their age and simplicity, integrate-and-fire models are still an extremely useful description of neuronal activity. By avoiding a biophysical description of the action potential, integrate-and-fire models are left with the simpler task of modeling only subthreshold membrane potential dynamics. This can be done with various levels of rigor. In the simplest version of these models, all active membrane conductances are ignored, and the entire membrane conductance is modeled as a single passive leakage term, $i_{\text{m}} = \overline{g}_{\text{L}}(V - E_{\text{L}})$. For small fluctuations about the resting membrane potential, neuronal conductances are approximately constant, and the passive integrate-and-fire model assumes that this constancy holds over the entire subthreshold range. For some neurons this is a reasonable approximation, and for others it is not. With these approximations, the model neuron behaves like an electronic circuit consisting of a resistor and a capacitor in parallel (figure 6.8A).

For the time being, we will ignore synaptic inputs by setting i_{s} to zero and concentrate on the effect of electrode currents. In this case, the membrane potential in the passive integrate-and-fire model is described by the basic equation of a single compartment model, 6.1, with a single passive membrane conductance,

$$c_{\text{m}} \frac{dV}{dt} = -\overline{g}_{\text{L}}(V - E_{\text{L}}) + \frac{I_{\text{e}}}{A} \,. \tag{6.21}$$

It is convenient to multiply this equation by the specific membrane resistance r_{m}, which is given by $r_{\text{m}} = 1/\overline{g}_{\text{L}}$ because the model has only a leakage conductance. This cancels the factor of $\overline{g}_{\text{L}}$ on the right side of the equation and leaves a factor $c_{\text{m}} r_{\text{m}} = \tau_{\text{m}}$ on the left side, where τ_{m} is the

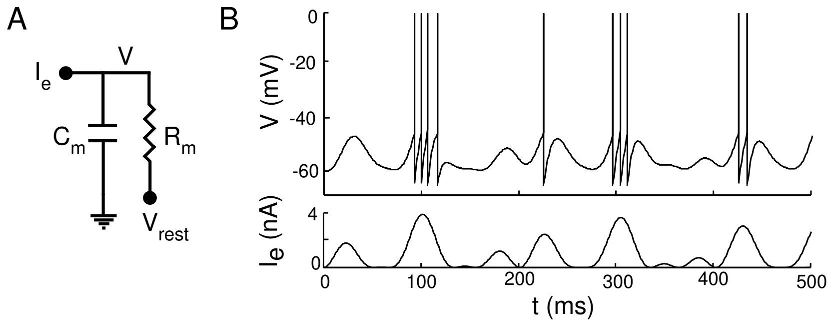

Figure 6.8: The passive integrate-and-fire model. A) The equivalent resistor-capacitor circuit. B) A passive integrate-and-fire model driven by a time-varying current. The upper trace is the membrane potential and the bottom trace the driving current. The action potentials in this figure are simply pasted onto the membrane potential trajectory when it reaches the threshold value. The parameters of the model are $E_L = -65$ mV, $V_{th} = -50$ mV, $V_{reset} = -70$ mV, $\tau_m = 10$ ms, and $R_m = 10$ MΩ.

membrane time constant of the neuron. The electrode current ends up being multiplied by r_m/A which is the total membrane resistance R_m. Thus, the basic equation of the passive integrate-and-fire models is

$$\tau_m \frac{dV}{dt} = E_L - V + R_m I_e \,. \tag{6.22}$$

Equation 6.22 is augmented by the rule that when V reaches the threshold value V_{th}, an action potential is fired and the potential is reset to V_{reset}. Equation 6.22 indicates that when $I_e = 0$, the membrane potential relaxes exponentially with time constant τ_m to $V = E_L$. E_L is thus the resting potential of the model cell. Figure 6.8B shows an example of an integrate-and-fire neuron driven by a time varying external current.

The firing rate of an integrate-and-fire model in response to a constant injected current can be computed analytically (methods for integrating equation 6.22 both analytically and numerically are discussed in Appendix A). When I_e is independent of time, the subthreshold potential $V(t)$ determined by equation 6.22 is

$$V(t) = E_L + R_m I_e + (V(0) - E_L - R_m I_e) \exp(-t/\tau_m) \tag{6.23}$$

where $V(0)$ is the value of V at time $t = 0$. This solution can be checked simply by substituting it into equation 6.22, but it is valid for the full integrate-and-fire model only as long as V stays below the threshold. Suppose that at $t = 0$, the neuron has just fired an action potential and is thus at the reset potential, so that $V(0) = V_{reset}$. The next action potential will occur when the membrane potential reaches the threshold, that is, at a time $t = T$ when

$$V(T) = V_{th} = E_L + R_m I_e + (V_{reset} - E_L - R_m I_e) \exp(-T/\tau_m) \,. \tag{6.24}$$

By solving this for T, the time of the next action potential, we can determine the interspike interval, or equivalently, its inverse, the firing rate of the neuron for constant I_e,

$$r = \frac{1}{T} = \left[\tau_m \ln\left(\frac{R_m I_e + E_L - V_{reset}}{R_m I_e + E_L - V_{th}}\right)\right]^{-1} . \tag{6.25}$$

This expression is valid if $R_m I_e > V_{th} - E_L$, otherwise the firing rate is zero. For large values of I_e, we can use the linear approximation of the logarithm ($\ln(1+z) \approx z$ for small z) to show that r grows linearly with I_e, $r \approx R_m I_e/(\tau_m(V_{th} - V_{reset}))$.

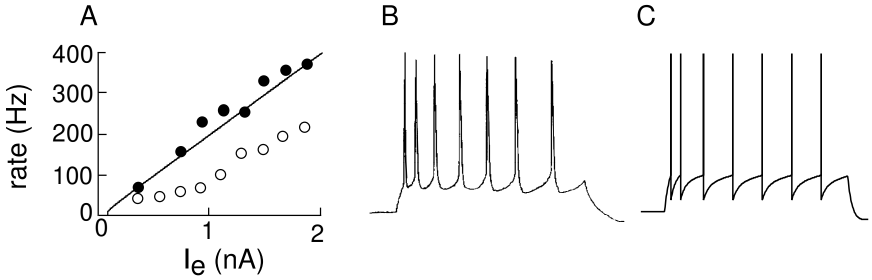

Figure 6.9: A) Comparison of firing rates as a function of injected current for an integrate-and-fire model and a cortical neuron measure *in vivo*. The line gives the firing rate of a model neuron with $\tau_m = 30$ ms, $V_{reset} = V_{rest} = -65$ mV, $V_{th} = -50$ mV and $R_m = 90$ MΩ. The data points are from a pyramidal cell in the primary visual cortex of a cat. The filled circles show the inverse of the interspike interval for the first two spikes fired, while the open circles show the steady-state firing rate after spike-rate adaptation. B) A recording of the firing of a cortical neuron under constant current injection showing spike-rate adaptation. C) Membrane voltage trajectory and spikes for an integrate-and-fire model with an added current with $r_m \Delta g_{sra}$ = 0.06, τ_{sra} = 100 ms, and E_K = -70 mV. Other parameters are as in figure 6.8. (Data in A from Ahmed *et al*, 1997, B from McCormick, 1990)

Figure 6.9A compares the firing rate as a function of I_e, using appropriate parameter values, with data from current injection into a cortical neuron *in vivo*. The firing rate of the cortical neuron in figure 6.9A has been defined as the inverse of the interval between pairs of spikes. The rates determined in this way using the first two spikes fired by the neuron in response to the injected current (filled circles in figure 6.9A) agree fairly well with the results of the integrate-and-fire model with the parameters given in the figure caption. However, the real neuron exhibits spike-rate adaptation, the interspike intervals lengthen over time when a constant current is injected into the cell (figure 6.9B) before settling to a steady-state value. The steady-state firing rate in figure 6.9A (open circles) could also be fit by an integrate-and-fire model, but not using the same parameters as were used to fit the initial spikes. Not all neurons show spike-rate adaptation, but consideration of this phenomenon allows us to show how the integrate-and-fire model can be modified to incorporate more complex dynamics.

Spike-Rate Adaptation and Refractoriness

The passive integrate-and-fire model that we have described is based on two approximations, a highly simplified description of the action potential and a linear approximation for the total membrane current. If details of the action potential generation process are not important for a particular modeling goal, the first approximation can be retained while the membrane current is modeled in as much detail as is necessary. We will illustrate this process by developing a heuristic description of spike-rate adaptation using a model conductance that has characteristics similar to measured neuronal conductances known to play important roles in producing this effect.

We model spike-rate adaptation by including an addition current in the model consider thus far,

$$\tau_{\mathrm{m}} \frac{dV}{dt} = E_{\mathrm{L}} - V - r_{\mathrm{m}} g_{\mathrm{sra}}(V - E_K) + R_{\mathrm{m}} I_{\mathrm{e}} \, . \tag{6.26}$$

The spike-rate adaptation conductance g_{sra} has been modeled as a K^+ conductance so, when activated, it will hyperpolarize the neuron, slowing any spiking that may be occurring. We assume that this conductance relaxes to zero exponentially with time constant τ_{sra} through the equation

$$\tau_{\mathrm{sra}} \frac{dg_{\mathrm{sra}}}{dt} = -g_{\mathrm{sra}} \, . \tag{6.27}$$

Whenever the neuron fires a spike, g_{sra} is increased by an amount Δg_{sra}, that is, $g_{\mathrm{sra}} \rightarrow g_{\mathrm{sra}} + \Delta g_{\mathrm{sra}}$. During repetitive firing, the current builds up in a sequence of steps causing the firing rate to adapt. Figures 6.9B and 6.9C compare the output of the model with the adapting firing pattern of a cortical neuron.

After a neuron fires an action potential, there is a short interval, called the absolute refractory period, during which it cannot fire a second spike. This is followed by a longer period, the relative refractory period, when action potentials are more difficult to evoke. Refractory effects are not included in the basic integrate-and-fire neuron, but they can be incorporated by adding a conductance like the spike-rate adaptation conductance, but with a faster recovery time and a larger conductance increment following an action potential. With a large increment, the current can essentially clamp the neuron to E_{K} following a spike and temporarily prevent further firing. As this conductance relaxes back to zero, firing will be possible, but initially less likely, due to its effects. When recovery is completed, normal firing can resume. An alternative scheme that is sometimes used to model refractory effects is to raise the threshold for action potential generation following a spike and then to allow it to relax back to its normal value.

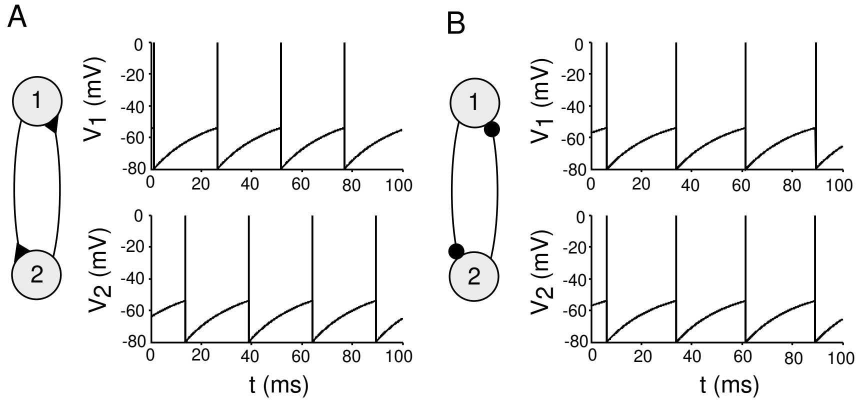

Figure 6.10: Two synaptically coupled integrate-and-fire neurons. A) Excitatory synapses (E_s = 0 mV) produce an alternating, out-of-phase pattern of firing. B) Inhibitory synapses (E_s = -80 mV) produce synchronous firing. Both model neurons have V_rest = -70 mV, V_th = -54 mV, V_reset = -80 mV, $r_\mathrm{m}\overline{g}_\mathrm{s}$ = 0.05, $R_\mathrm{m}I_\mathrm{e}$ = 25 mV, and τ_s = 10 ms.

Adding Synaptic Conductances

Up to now, we have ignored synaptic conductances in the models we have been discussing. Synaptic inputs are incorporated into a conductance-based model by including synaptic conductances (as described in chapter 5) in the synaptic current appearing in equation 6.1. Equivalently, for an integrate-and-fire model a synaptic conductance term is added to equation 6.22,

$$\tau_\mathrm{m}\frac{dV}{dt} = E_\mathrm{L} - V - r_\mathrm{m}\overline{g}_\mathrm{s}s(V - E_\mathrm{s}) + R_\mathrm{m}I_\mathrm{e}\,. \tag{6.28}$$

The synaptic conductance is written as the product of a fixed maximal conductance $\overline{g}_\mathrm{s}$and a dynamic gating variable s. The synaptic current is multiplied by r_m in equation 6.28 because equation 6.22 was multiplied by this factor. To model synaptic transmission, s changes whenever the presynaptic neuron fires an action potential. Various ways of describing and computing s are discussed in chapter 5.

Figures 6.10A and 6.10B show examples of two integrate-and-fire neurons connected by identical excitatory or inhibitory synapses. The synaptic conductances in this example are described by the α function model discussed in chapter 5. This means that the synaptic conductance a time t after the occurrence of a presynaptic action potential is given by $s = (t\tau_s)\exp(-t/\tau_s)$ (see chapter 5 for methods of implementing this model). The figure shows an interesting effect first noted by Rinzel and Wang (1992) and further analyzed by Van Vreeswijk, Ermentrout, and Abbott (1994). When the synaptic time constant is sufficiently long (τ_s = 10 ms in this example), excitatory connections produce a state in which the two neurons fire alternately, out of phase with each other. Inhibitory synapses produces synchronous firing. This is a fairly general, though somewhat counterintuitive, phenomenon. Inhibitory connections are often more effective than excitatory connections at synchronizing neuronal firing (see exercise xx for further analysis).

Synapses have multiple effects on their postsynaptic targets. To identify these effects it is useful to express the membrane potential in terms of a deviation v from its resting value by writing $V = E_{\rm L} + v$. Expressed as an equation for v, equation 6.28 then becomes

$$\frac{\tau_{\rm m}}{1 + r_{\rm m}\overline{g}_{\rm s}s}\frac{dv}{dt} = -v + \frac{r_{\rm m}\overline{g}_{\rm s}s(E_{\rm s} - E_{\rm L}) + R_{\rm m}I_{\rm e}}{1 + r_{\rm m}\overline{g}_{\rm s}s}\,.. \tag{6.29}$$

For constant $I_{\rm e}$, v approaches the stead-state value

$$v_\infty = \frac{r_{\rm m}\overline{g}_{\rm s}s(E_{\rm s} - E_{\rm L}) + R_{\rm m}I_{\rm e}}{1 + r_{\rm m}\overline{g}_{\rm s}s} \tag{6.30}$$

exponentially with time constant $\tau_{\rm m}/(1 + r_{\rm m}\overline{g}_{\rm s}s)$. This result illustrates three different, but related, effects of the synapse. The term proportional to the synaptic conductance in the numerator of equation 6.30 represents a source of current that is added to the external current. The term in the denominator of equation 6.30 shows a divisive effect of the synapse. This term also appears in the effective time constant $\tau_{\rm m}/(1 + r_{\rm m}\overline{g}_{\rm s}s)$, which is lengthenned by the synaptic conductance. Some inhibitory synapses have $E_{\rm s} \approx E_{\rm L}$ so their dominant effect in equation 6.30 is divisive. Such synapses are called shunting, and they provide a possible biophysical basis for the divisive normalization of visual responses discussed in chapter 2. Shunting synapses have also been used in a number of models when a divisive rather than a subtractive effect of inhibition is needed.

Regular and Irregular Firing Modes

Integrate-and-fire models are useful for studying how neurons integrate large numbers of synaptic inputs and how networks of neurons interact. Softky and Koch (1992 & 1994) raised an interesting issue concerning the variability of the response of an integrate-and-fire neuron receiving a large number of synaptic inputs. This led to the realization that neurons can respond to multiple synaptic inputs in two different modes of operation (Troyer and Miller, 1997; Bugmann *et al*, 1997) depending on the balance that exists between excitatory and inhibitory inputs (Shadlen and Newsome, 1994).

The two modes of operation are illustrated in figure 6.11, which shows membrane potentials of an integrate-and-fire model neuron responding to 1000 excitatory and 200 inhibitory inputs. Each input consists of an independent Poisson spike train driving a synaptic conductance. The upper

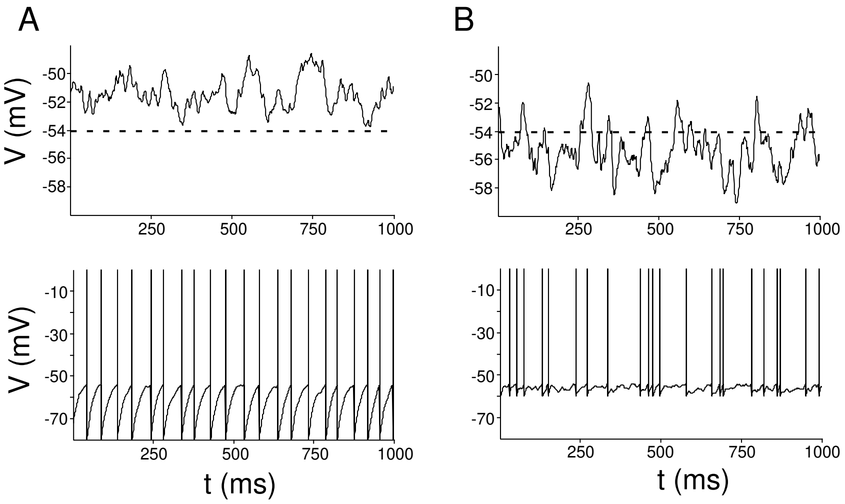

Figure 6.11: The regular and irregular firing modes of an integrate-and-fire model neuron. A) The regular firing mode. Upper panel: The membrane potential of the model neuron when the spike generation mechanism is turned off. The average membrane potential is above the spiking threshold (dashed line). Lower panel: When the spike generation mechanism is turned on, it produces a regular spiking pattern. B) The irregular firing mode. Upper panel: The membrane potential of the model neuron when the spike generation mechanism is turned off. The average membrane potential is below the spiking threshold (dashed line). Lower panel: When the spike generation mechanism is turned on, it produces an irregular spiking pattern. In order to keep the firing rates comparable in these two examples, the value of the reset voltage is higher and the membrane time constant is smaller in B than in A.

panels of figure 6.11 show the membrane potential with the action potential generation mechanism of the model turned off, and figures 6.11A and 6.11B illustrate the two different modes of operation. In figure 6.11A, the effect of the excitatory inputs is strong enough, relative to that of the inhibitory inputs, to make the average membrane potential, when action potential generation is blocked, more depolarized than the spiking threshold of the model (the dashed line in the figure). When the action potential mechanism is turned on (lower panel of figure 6.11A), this produces a fairly regular pattern of action potentials.

The irregularity of a spike train can be quantified using the coefficient of variation (C_V), the ratio of the standard deviation to the mean of the interspike intervals (see chapter 1). For the Poisson inputs being used in this example, $C_V = 1$, while for the spike train in the lower panel of figure 6.11A, $C_V = 0.16$. Thus, the output spike train is much more regular than the input trains. This is not surprising, because the model neuron effectively averages its many synaptic inputs. In the regular firing mode, the total synaptic input attempts to charge the neuron above the threshold, but every time the potential reaches the threshold it gets reset and starts charging again. In this mode of operation, the timing of the action potentials is determined primarily by the charging rate of the cell, which is controlled by its membrane time constant.

Figure 6.11B shows the other mode of operation that produces an irregular firing pattern. In the irregular firing mode, the average membrane potential is more hyperpolarized than the threshold for action potential generation (upper panel of figure 6.11B). Action potentials are only generated when there is a fluctuation in the total synaptic input strong enough to make the membrane potential reach the threshold. This produces an irregular spike train, such as that seen in the lower panel of figure 6.11B which has a C_V value of 0.84.

The high degree of variability seen in the spiking patterns of *in vivo* recordings of cortical neurons suggests that they are better approximated by an integrate-and-fire model operating in an irregular-firing mode (see chapter 1). There are advantages to operating in the irregular-firing mode that may compensate for its increased variability. One is that neurons firing in the irregular mode reflect in their outputs the temporal properties of fluctuations in their total synaptic input. In the regular firing mode, the timing of output spikes is only weakly related to the temporal character of the input spike trains. In addition, neurons operating in the irregular firing mode can respond more quickly to changes in presynaptic spiking patterns and firing rates than those operating in the regular firing mode.

6.3 Multi-Compartment Models

The single-compartment models we have discussed to this point cannot represent the morphological structure of real neurons. To do this we need to use multiple compartments. It is possible to construct models with many compartments that reflect the morphology of a given neuron with great accuracy. Each compartment in such a model may have a number of different conductances, resulting in a large number of free parameters, in particular the maximal conductances for the currents within each compartment. At present, these are by no means fully constrained by experimental data. Nevertheless, more information concerning the distribution of conductances in real neurons is becoming available, and with some assumptions about these distributions, multi-compartment models can provide key insights concerning the role of morphology and channel distributions in the generation of neuronal responses.

In a multi-compartment model, each compartment has its own membrane potential V_μ (where μ labels compartments), and its own gating variables that determine the membrane current for compartment μ, $i_{\rm m}^{(\mu)}$. Each membrane potential V_μ satisfies an equation similar to (6.1) except that the compartments couple to their neighbors in the multi-compartment structure. For a nonbranching cable, each compartment is coupled to two neighbors,

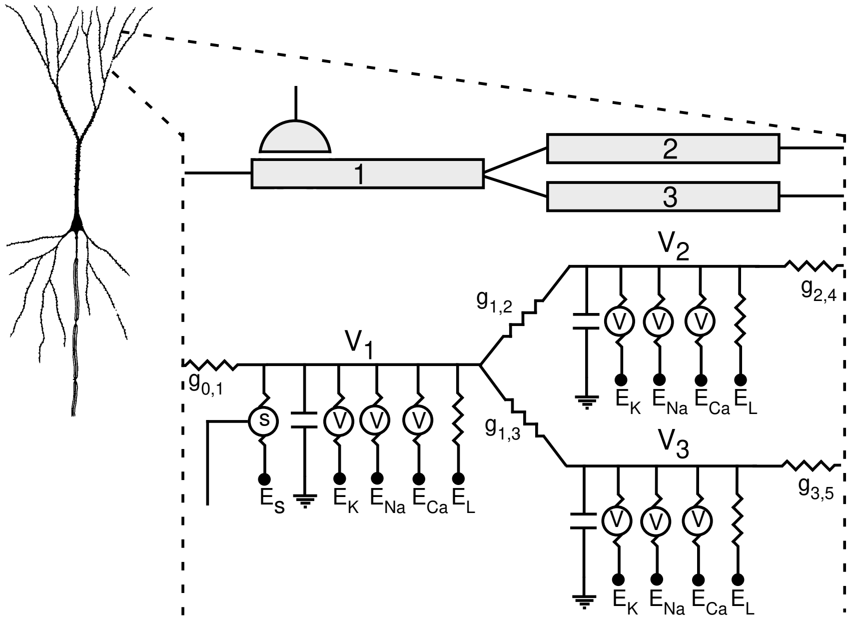

Figure 6.12: A multi-compartment model of a neuron. The expanded region shows three compartments at a branch point where a single cable splits into two. Each compartment has membrane and synaptic conductances, as indicated by the equivalent electrical circuit, and the compartments are coupled together by resistors.

and the equations for the membrane potentials of the compartments have the form

$$\begin{aligned} c_{\mathrm{m}}\frac{dV_\mu}{dt} &= -\sum_i g_i^\mu (V - E_i) + I_{\mathrm{e}}^\mu / A_\mu \\ &\quad + g_{\mu,\mu+1}(V_{\mu+1} - V_\mu) + g_{\mu,\mu-1}(V_{\mu-1} - V_\mu)\,. \end{aligned} \tag{6.31}$$

For a compartment at the end of a cable, there is only one neighboring compartment, and thus only a single term in the bottom line of equation 6.31. For a compartment where a cable branches in two, there are three terms corresponding to coupling of the branching node to the first compartment in each daughter branch.

The constant $g_{\mu,\mu'}$ that determines the resistive coupling between neighboring compartments μ and μ' are determined by computing the current that flows between two neighboring compartments due to Ohm's law. For simplicity, we begin by computing the coupling between two compartment that have the same length L and radius a. Using the results of chapter 5, the resistance between two such compartments, measured from their centers, is the intracellular resistivity, r_{L} times the distance between the compartment centers divided by the cross-sectional area, $r_{\mathrm{L}}L/\pi a^2$. The total current flowing between compartment $\mu + 1$ and compartment μ is then $\pi a^2(V_{\mu+1} - V_\mu)/r_{\rm L}L$. Recall that equation 6.1 for the potential within a single compartment refers to currents per unit area of membrane. Thus, in the equation for compartment μ of a multi-compartment model we must divide the total current from compartment μ' by the surface area of compartment μ, $2\pi aL$. Thus, we find that $g_{\mu,\mu'} = a/(2r_{\rm L}L^2)$.

The value of $g_{\mu,\mu'}$ is given by a more complex expression if the two neighboring compartments have different lengths or radii. This can occur when a tapering cable is approximated by a sequence of cylindrical compartments, or at a branch point where a single compartment connects with two other compartments as in figure 6.12. In either case, suppose that compartment μ has length L_μ and radius a_μ and compartment μ' has length $L_{\mu'}$ and radius $a_{\mu'}$. The resistance between these two compartments is the sum of the two resistances from the middle of each compartment to the junction between them, $r_{\rm L}L_\mu/(2\pi a_\mu^2) + r_{\rm L}L_{\mu'}/(2\pi a_{\mu'}^2)$. To compute $g_{\mu,\mu'}$ we divide this by the total surface area of compartment μ, $2\pi a_\mu L_\mu$, which gives

$$g_{\mu,\mu'} = \frac{a_\mu a_{\mu'}^2}{r_{\rm L}L_\mu(L_\mu a_{\mu'}^2 + L_{\mu'}a_\mu^2)} \,. \tag{6.32}$$

Equations such as 6.31 for all of the compartments of a model neuron determine the membrane potential throughout the neuron with a spatial resolution given by the compartment size. An efficient method for integrating equation 6.31 is discussed in Appendix C. Using this scheme, models can be numerically integrated extremely efficiently, even those involving large numbers of compartments. Such integration schemes are built into neuron simulation software packages such as Neuron and Genesis.

Action Potential Propagation Along an Unmyelinated Axon

As an example of multi-compartment modeling, we simulate the propagation of an action potential along an unmyelinated axon using the currents measured in the squid giant axon by Hodgkin and Huxley. In the Hodgkin-Huxley model, $i_{\rm m}$ is the sum of three currents, a leakage current, a delayed-rectifier $\mathtt{K}^+$ current, and a transient $\mathtt{Na}^+$ current, and these depend on three dynamic variables m, h and n. Specifically,

$$i_{\rm m} = \overline{g}_{\rm L}(V - E_{\rm L}) + \overline{g}_{\rm K}n^4(V - E_{\rm K}) + \overline{g}_{\rm Na}m^3h(V - E_{\rm Na}) \tag{6.33}$$

where $\overline{g}_L = 3\ \mu\text{S/mm}^2$, $\overline{g}_K = 360\ \mu\text{S/mm}^2$, $\overline{g}_{Na} = 1200\ \mu\text{S/mm}^2$, $E_{\rm L}$ = -54.402 mV, $E_{\rm K}$ = -77 mV and $E_{\rm Na}$ = 50 mV. The dynamic equations for the variables m, h, and n are given in chapter 5. Figure 6.13 shows an action potential propagating along an axon with each compartment modeled in this way. The action potential extends over more than 1 mm of axon and it travels at a speed of about 2 mm/ms or 2 m/s.

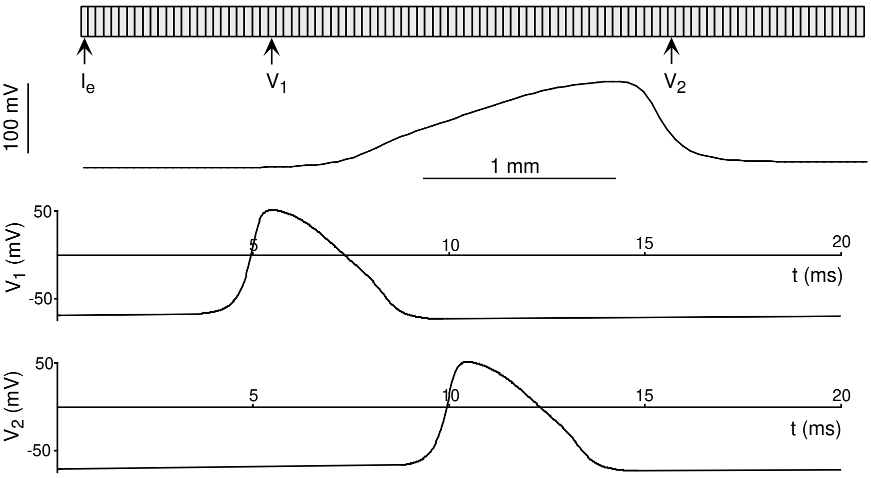

Figure 6.13: Propagation of an action potential along a multi-compartment model axon. The upper panel shows the multi-compartment representation of the axon with 100 compartments. The axon segment shown is 4 mm long and has a radius of 1 μm. An external current sufficient to initiate action potentials is injected at the point marked I_e. The panel beneath this shows the membrane potential as a function of position along the axon, at a given instant of time. The spatial position in this panel is aligned with the axon depicted above it. The action potential is moving to the right. The bottom two panels show the membrane potential as a function of time at the two locations denoted by the arrows and symbols V_1 and V_2 in the upper panel.

Propagation Along a Myelinated Axon

Many axons in vertebrates are covered with an insulating sheath of myelin except at gaps, called the nodes of Ranvier, where voltage-dependent ion channels (primarily $\mathtt{Na}^+$ channels) are concentrated (see figure 6.14A). Action potentials propagate passively down the myelin-covered sections of the axon and are actively regenerated at the nodes of Ranvier. The myelin sheath consists of many layers of membrane wrapped around the axon. This greatly increases the membrane resistance and greatly decreases the capacitance of the covered segment of the axon. Figure 6.14 shows the equivalent circuit for a multi-compartment model of a myelinated axon.

We can compute the membrane resistance of a myelin covered axon by treating the myelin sheath as an extremely thick cell membrane. Consider the geometry shown in the cross-sectional diagram of figure 6.14B. The myelin sheath extends from the radius a_1 of the axon core to the outer radius a_2. If the thickness of a single layer of cell membrane is d_m, the specific membrane resistance per unit membrane thickness is r_m/d_m, where r_m is the specific membrane resistance introduced in chapter 5. The membrane resistance of a cylindrical shell of membrane with thickness Δa, radius a, and length Δx is the specific membrane resistance per unit thickness times the thickness of the shell divided by the area of the shell, which is

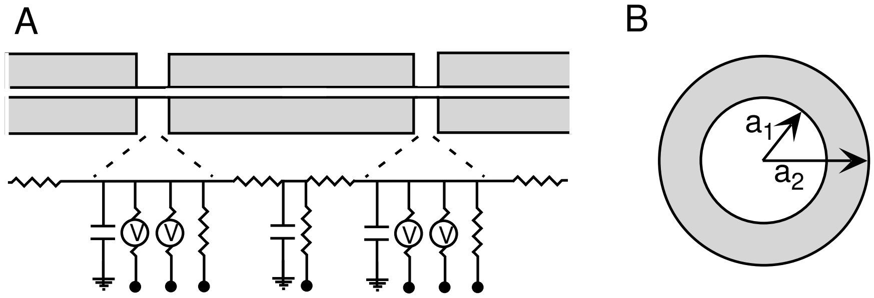

Figure 6.14: A myelinated axon. A) The equivalent circuit for a multi-compartment representation of a myelinated axon. The myelinated segments are represented by a membrane capacitance, a passive membrane resistance, and a longitudinal resistance. The nodes of Ranver contain voltage-dependent conductances (primarily $\mathtt{Na}^+$ with some $\mathtt{K}^+$) as well. B) A cross-section of a myelinated axon consisting of a central axon core of radius a_1 and a myelin sheath making a total outside radius of a_2.

$r_\mathrm{m}\Delta a/(d_\mathrm{m}2\pi a\Delta x)$. The total membrane resistance of a length Δx of myelinated axon is obtained by taking the limit $\Delta a \to 0$ and integrating over the thickness of the sheath,

$$R_\mathrm{m} = \frac{r_\mathrm{m}}{d_\mathrm{m}2\pi\Delta x}\int_{a_1}^{a_2}\frac{da}{a} = \frac{r_\mathrm{m}\ln(a_2/a_1)}{d_\mathrm{m}2\pi\Delta x}\,. \tag{6.34}$$

A similar calculation of the membrane capacitance for this length of axon gives the result $C_\mathrm{m} = c_\mathrm{m}d_\mathrm{m}2\pi\Delta x/\ln(a_2/a_1)$, so we see that the membrane resistance and membrane capacitance are scaled by inverse factors. This means that the membrane time constant $\tau_\mathrm{m} = R_\mathrm{m}C_\mathrm{m} = r_\mathrm{m}c_\mathrm{m}$ is not affected by the myelination. The longitudinal resistance of this length of axon, $R_\mathrm{L} = r_\mathrm{L}\Delta x/(\pi a_1^2)$, is also unaffected by the myelination, because longitudinal current flows only inside the central core.

The calculations done in the previous paragraph can be used to determine the optimal thickness of myelination for an axon of fixed outside diameter. Specifically, we can determine the core diameter a_1 that gives the maximum action potential propagation speed if an axon is required to fit within a space of radius a_2. As shown in chapter 5, the effective speed of propagation down a passive cable is $2\lambda/\tau_\mathrm{m}$, where λ is the length constant of the cable. Because myelination has no effect on the membrane time constant τ_m, we must choose a_1 to make the length constant λ as big as possible to maximize this propagation speed. In chapter 5, we showed that the length constant for an unmyelinated axon was given by $\lambda^2 = ar_\mathrm{m}/(2r_\mathrm{L})$. A review of this derivation shows that the generalization to the myelinated case is

$$\lambda^2 = \frac{(\Delta x)^2 R_\mathrm{m}}{R_\mathrm{L}} = \frac{r_\mathrm{m}a_1^2\ln(a_2/a_1)}{2d_\mathrm{m}r_\mathrm{L}}\,. \tag{6.35}$$

To determine the inner radius that maximizes this length constant, we set the derivative of this expression with respect to a_1 to zero. This gives the result $a_1 = a_2 \exp(-1/2)$ or $a_1 = 0.6a_2$. An inner core fraction of 0.6 is typical for myelinated axons, indicating that the thickness of myelin is indeed optimal.

6.4 Firing-Rate Models

The models we have discussed thus far produce spike sequences deterministically in response to injected current or synaptic input. Sequences of action potentials produced by these models can only be compared with those of real neurons if the total synaptic input to the real neuron is known, and this is rarely the case. If the synaptic input is not known, it may only be possible to perform statistical comparisons of a model with the data. For example, a model may fail to predict exact spike sequences, although it adequately predicts firing rates. In this case, a simpler model that is couched in terms of firing rates rather than spike sequences may provide a sufficient description. Such models were discussed in chapters 1 and 2, where we also discussed methods of generating spike trains stochastically from them.

Single neuron models are the basic building blocks for constructing models of neural circuits and networks. In a network model, we are primarily concerned with faithfully reproducing the dynamics of the circuit being modeled. Network dynamics is affected both by the response properties of individual neurons and by the synaptic connections between neurons. Thus, in addition to reproducing individual neuronal responses, a single neuron model used within a network must generate realistic synaptic inputs to other neurons. Here models that produce sequences of spikes have a distinct advantage because the spike sequences can be fed into a model of synaptic conductances to produce realistic synaptic input. Nevertheless, reduced models that deal exclusively with firing rates, rather than generating spike sequences, are used extensively in network modeling because of their ease of analysis and because, in some regimes at least, they are adequately similar to their spiking counterparts. For example, firing-rate models form the basis for the discussions of network models, adaptation, and learning in the following chapters. In this section, we introduce firing-rate models of neural networks and discuss the assumptions upon which they are based. These models make most sense in the case that there are many, interconnected, neurons. We therefore treat this case formally. In the next chapter we consider some computational properties of the resulting dynamical system.

Consider a network of N neurons that will be described by firing rates r_a with $a = 1, 2, \ldots, N$. If neuron b fires at time zero, we write the post-synaptic potential observed at the cell body of neuron a (the somatic potential) at time t as $M_{ab}K(t)$. Writing it like this implies that we are ignoring any voltage-dependence in the conductances and the dendrites. M_{ab} describes the amplitude and sign of the post-synaptic potential generated in neuron a by neuron b, and $K(t)$ describes its time course. To avoid an ambiguity in the definition of M_{ab}, we normalize $K(t)$ by requiring its integral over all positive times to be one. For simplicity at this point, we use the same function $K(t)$ to describe all synapses.

Assuming linearity, the total somatic potential of neuron a at time t due to a sequence of presynaptic spikes at synaptic terminal b occurring at times t_i is the sum

$$M_{ab} \sum_{t_i < t} K(t - t_i) = M_{ab} \int_0^\infty d\tau \, K(\tau) \rho_b(t - \tau) \, . \tag{6.36}$$

On the right side of this equation, we have used the neural response function introduced in chapter 1, $\rho_b(t) = \sum_i \delta(t - t_i)$, to describe the sequence of spikes fired by neuron b. The equality follows from integrating over the sum of δ functions in the definition of $\rho_b(t)$. The total synaptic contribution to the potential at the cell body of neuron a, $V_a(t)$ is obtained by summing the contributions from all of its synaptic inputs,

$$V_a(t) = \sum_{b=1}^{N} M_{ab} \int_0^\infty d\tau \, K(\tau) \rho_b(t - \tau) \tag{6.37}$$

$$= \int_0^\infty d\tau \, K(\tau) \sum_{b=1}^{N} M_{ab} \rho_b(t - \tau) \, . \tag{6.38}$$

In a spiking model such as the integrate-and-fire model we considered above, the synaptic contribution to this potential should be augmented by a term to take account of the reset of the cell to V_{reset} following the emission of a spike. The spike response model (see Gerstner, 1998), which is a generalisation of the integrate-and-fire model, takes explicit account of these extra terms in order to study aspects of the very short-term behavior of networks of neurons. Standard firing rate models ignore it, and instead make two critical approximations. One is to replace $\rho_b(t)$, which is a sum of a set of delta functions, with its trial-based average

$$\rho_b(t) \approx \langle \rho_b(t) \rangle = p_b(t) \tag{6.39}$$

where $p_b(t)$ is the instantaneous firing rate of neuron b. The second approximation is that the firing rate of neuron b, in the form of the instantaneous spike probability, $p_b(t)$, is related to the membrane potential by the instantaneous equation:

$$p_b(t) = F(V_b(t)) \tag{6.40}$$

where function F will be specified later. Some conditions under which these approximations are both close and far are known. Very crudely, they are safe away from either very fast firing rates or very short-term behavior of the cells (such as synchronization of individual spikes). They rely on a form of mean-field approximation used in statistical physics, that the variability across a large number of inputs effectively reproduces the trial-to-trial variability for any single input, so the sum over synaptic inputs effectively averages out the trial-to-trial variability on any one of them.

The two forms of $V_a(t)$ in equations 6.37 and 6.38 lead to two slightly different dynamical equations for the evolution of the rates, which are based on different assumptions about the longer of two timescales, for the *synapse* or for the *membrane* (Ermentrout, 1998). The form in equation 6.37 is best interpreted in the case that the dynamics of the membrane are fast compared with those of the synapse, or the cell sits so close to its spiking threshold that little integration by the membrane is required. In this case, the membrane principally acts to add the contributions from the synapses, which themselves are synaptically filtered versions of the presynaptic activity. Write

$$U_b(t) = \int_0^\infty d\tau\, K(\tau) p_b(t-\tau) = \int_{-\infty}^t d\tau\, K(t-\tau) p_b(\tau)\ , \tag{6.41}$$

for the integral in equation 6.37. Note that $U_b(t)$ is an appropriate candidate for $r_b(t)$, which is a temporally *smoothed* version of the firing rate of neuron b, and so we use $r_b(t)$ in its place. Applying equations 6.40 and 6.41 to neuron a, we get

$$r_a(t) = \int_{-\infty}^t d\tau\, K(t-\tau) p_a(\tau) = \int_{-\infty}^t d\tau\, K(t-\tau) F\left(\sum_{b=1}^N M_{ab} r_b(\tau)\right) \tag{6.42}$$

If a synapse can be treated as a simple low pass filter with a time constant τ_s, *ie*

$$K(\tau) = \frac{1}{\tau_s} e^{-\frac{\tau}{\tau_s}} \tag{6.43}$$

then we can differentiate equation 6.42 to get

$$\tau_s \frac{d}{dt} r_a(t) = -r_a(t) + F\left(\sum_{b=1}^N M_{ab} r_b(t)\right) \tag{6.44}$$

If the synaptic contribution to the potential is held constant, r_a approaches the value $F(\sum M_{ab} r_b)$, so F is the steady-state firing rate as a function of synaptic current. It is often modeled as a threshold linear function $F(\sum M_{ab} r_b) = [\sum M_{ab} r_b - \Theta]_+$, where Θ is the threshold voltage and, as in previous chapters, the notation $[\,]_+$ denotes rectification. Alternatively, F is often modeled as a saturating function such as a sigmoidal function. Sometimes an external input h_a to neuron a is included by writing $F(h_a + \sum M_{ab} r_b)$ in equation 6.44.

The form of the integral equation 6.38 suggests an alternative interpretation in the case that the synapses are fast compared with the membrane.

Then, the synaptic input $\sum_{b=1}^{N} M_{ab}\rho_b(t)$ is filtered by the membrane $K(\tau) = \frac{1}{\tau_m}e^{-\frac{\tau}{\tau_m}}$ with the membrane time constant τ_m, leading, using equation 6.40, to

$$V_a(t) = \int_{-\infty}^{t} d\tau \, K(t-\tau) \sum_{b=1}^{N} M_{ab} F\left(V_b(\tau)\right) \; . \tag{6.45}$$

Differentiating this gives

$$\tau_m \frac{d}{dt} V_a(t) = -V_a(t) + \sum_{b=1}^{N} M_{ab} F\left(V_b(t)\right) \tag{6.46}$$

The firing rate of cell a is $p_a(t) = F(V_a(t))$. Since equation 6.46 is essentially a low pass filter, again we can equate this with a smoothed firing rate $r_a(t)$. Equation 6.46 is sometimes called the membrane potential form of the firing rate equation, whereas equation 6.44 is called the activity form. Multiplying equation 6.44 by matrix M and writing $\tilde{V}_a(t) = \sum_{b=1}^{N} M_{ab} r_b(t)$, we get

$$\tau_s \frac{d}{dt} \tilde{V}_a(t) = -\tilde{V}_a(t) + \sum_{b=1}^{N} M_{ab} F\left(\tilde{V}_b(t)\right) \tag{6.47}$$

just as in equation 6.46 (though with a different time constant). The dynamical behaviors of the two equations are therefore very closely related.

Paired Excitatory and Inhibitory Neurons

Some models use a single *pair* of an excitatory and an inhibitory cell as their basic computational unit. This can take better account of the neural separation between excitation and inhibition, even though such strict pairing is not actually present. Following Wilson & Cowan (1972), we analyse the range of basic dynamical behaviors of such pairs using the firing rate formulation. We consider the case of a single pair, with the firing rate of the excitatory cell being r_{E} and the inhibitory cell being r_{I}; although this might more reasonably come from a population of pairs, with identical firing rates.

In this example, the excitatory and inhibitory synapses are allowed to have different time constants, τ_{E} and τ_{I}, and the excitatory and inhibitory firing rates are defined using exponential kernels with these time constants. The recurrent synaptic strength from the excitatory neuron to itself is denoted by M_{EE}, from the inhibitory neuron to itself by M_{II}, from the inhibitory to the excitatory neuron by M_{EI}, and from the excitatory to the inhibitory neuron by M_{IE}. Using threshold linear response functions, and equation 6.44, the firing rates are determined by

$$\tau_{\mathrm{E}} \frac{dr_{\mathrm{E}}}{dt} = -r_{\mathrm{E}} + \left[M_{\mathrm{EE}} r_{\mathrm{E}} + M_{\mathrm{EI}} r_{\mathrm{I}} - \Theta_{\mathrm{E}}\right]_+ \tag{6.48}$$

and

$$\tau_{\mathrm{I}} \frac{dr_{\mathrm{I}}}{dt} = -r_{\mathrm{I}} + [M_{\mathrm{II}} r_{\mathrm{I}} + M_{\mathrm{IE}} r_{\mathrm{E}} - \Theta_{\mathrm{I}}]_+ \, . \tag{6.49}$$

In the example we consider, we set $M_{\mathrm{EE}} = 1.25$, $M_{\mathrm{IE}} = 1$, $M_{\mathrm{II}} = M_{\mathrm{EI}} = -1$, $\Theta_{\mathrm{E}} = -10$ Hz, $\Theta_{\mathrm{I}} = 10$ Hz, $\tau_{\mathrm{E}} = 10$ ms, and we vary the value of τ_{I}. The negative value of Θ_{E} means that this parameter serves as a source of background activity (activity in the absence of excitatory input) rather than as a threshold.

Phase-Plane Methods and Stability Analysis

The model of the pair of interacting excitatory and inhibitory cells given by equations 6.48 and 6.49 provides an opportunity to illustrate some of the techniques used to study the dynamics of nonlinear systems. This model exhibits both static (constant r_{E} and r_{I}) and oscillatory activity depending on the values of its parameters. Stability analysis can be used to determine the parameter values where transitions between these two types of activity take place.

The firing rates $r_{\mathrm{E}}(t)$ and $r_{\mathrm{I}}(t)$ arising from equations 6.48 and 6.49 can be displayed by plotting them as functions of time, as in figures 6.16A and 6.17A. Another useful way of depicting these results, illustrated in figures 6.16B and 6.17B, is to plot pairs of points $(r_{\mathrm{I}}(t), r_{\mathrm{E}}(t))$ for all relevant t values. As the firing rates change, these points trace out a curve or trajectory in the r_{E}-r_{I} plane, which is called the phase plane of the model. Phase-plane plots can be used to give a geometric picture of the dynamics of a model.

The values of r_{E} and r_{I} for which the right sides of either equation 6.48 or equation 6.49 vanish are of particular interest in phase-plane analysis. These sets of values form two curves in the phase plane known as nullclines. The nullclines for equations 6.48 and 6.49 are the straight lines drawn in figure 6.15A. The nullclines are interesting because they divide the phase plane into regions with opposite flow patterns. This is because the right side of equation 6.48 or equation 6.49 is positive on one side of its nullcline and negative on the other. The right sides of these equations determine the sign and magnitude of the rate of change of the corresponding firing rate, and thus set the direction of flow in the phase plane. These flow directions are denoted by horizontal and vertical arrows in figure 6.15A. Thus, above the nullcline along which $dr_{\mathrm{E}}/dt = 0$, $dr_{\mathrm{E}}/dt < 0$, and below it $dr_{\mathrm{E}}/dt > 0$. Similarly, $dr_{\mathrm{I}}/dt > 0$ to the right of the nullcline where $dr_{\mathrm{I}}/dt = 0$, and $dr_{\mathrm{I}}/dt < 0$ to the left of it.

A fixed point is a pair of firing rates that make $dr_{\mathrm{E}}/dt = dr_{\mathrm{I}}/dt = 0$. Since both derivatives vanish, these values will remain fixed in time. Because a fixed point requires both derivatives to vanish, it can only occur at an intersection of nullclines. The model we are considering has a single fixed

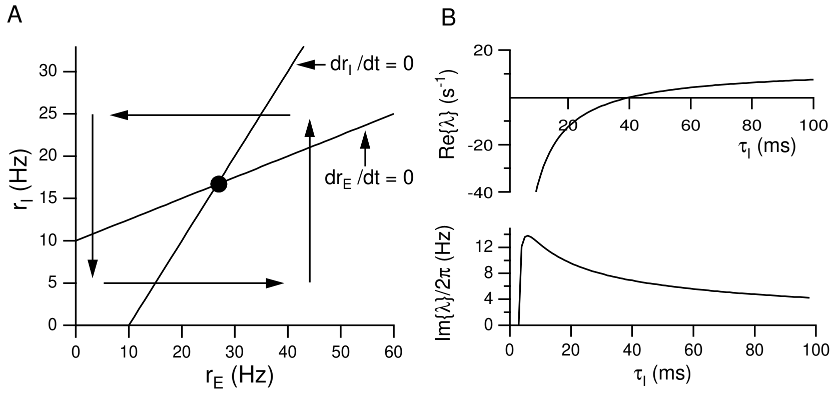

Figure 6.15: A) Nullclines, flow directions, and fixed point for the firing-rate model of interacting excitatory and inhibitory populations. The two straight lines are the nullclines along which $dr_E/dt = 0$ or $dr_I/dt = 0$. The filled circle is the fixed point of the model. The horizontal and vertical arrows indicate the directions that r_E (horizontal arrows) and r_I (vertical arrows) flow in different regions of the phase plane relative to the nullclines. B) Real (upper panel) and imaginary (lower panel) parts of the eigenvalue determining the stability of the fixed point. To the left of the point where the imaginary part of the eigenvalue goes to zero, both eigenvalues are real. The imaginary part has been divided by 2π to give the frequency of oscillations near the fixed point.

point denoted by the filled circle in figure 6.15A. A fixed point provides a potential static configuration for the system, but it is critically important whether the fixed point is stable or unstable. If a fixed point is stable, initial values of r_E and r_I near the fixed point will be drawn toward it over time. If the fixed point is unstable, nearby configurations are pushed away from the fixed point, and the system will only remain at the fixed point indefinitely if the rates are set initially to the fixed-point values with infinite precision.

Linear stability analysis (see chapter 12) can be used to determine whether the fixed point is stable or unstable. This analysis starts by considering the first derivatives of the right sides of equations 6.48 and 6.49 with respect to r_E and r_I evaluated at the values of r_E and r_I corresponding to the fixed point. The four combinations of derivatives computed in this way can be arranged into a matrix

$$\begin{pmatrix} (M_{EE} - 1)/\tau_E & M_{EI}/\tau_E \\ M_{IE}/\tau_I & (M_{II} - 1)/\tau_I \end{pmatrix} . \tag{6.50}$$

As discussed in chapter 12, the stability of the fixed point is determined by the eigenvalues of this matrix. The computation of these eigenvalues is

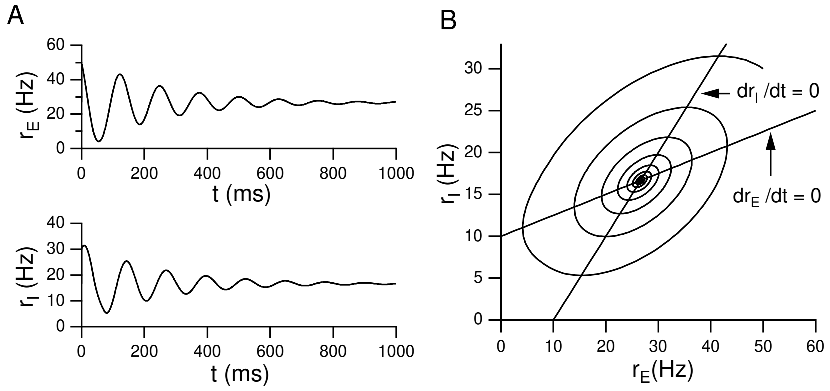

Figure 6.16: Activity of the excitatory-inhibitory firing-rate model when the fixed point is stable. A) The excitatory and inhibitory firing rates settle to the fixed point over time. B) The phase-plane trajectory is a counter-clockwise spiral collapsing to the fixed point. For this example, $\tau_{\mathrm{I}} = 30$ ms, and all other parameters are as given in the text.

discussed in chapter 12. They are given by

$$\lambda = \frac{1}{2}\left(\frac{M_{\mathrm{EE}}-1}{\tau_{\mathrm{E}}} + \frac{M_{\mathrm{II}}-1}{\tau_{\mathrm{I}}} \pm \sqrt{\left(\frac{M_{\mathrm{EE}}-1}{\tau_{\mathrm{E}}} - \frac{M_{\mathrm{II}}-1}{\tau_{\mathrm{I}}}\right)^2 + 4\frac{M_{\mathrm{EI}}M_{\mathrm{IE}}}{\tau_{\mathrm{E}}\tau_{\mathrm{I}}}}\right) \tag{6.51}$$

The stability of the fixed point is determined by the real parts of these eigenvalues (see chapter 12). If both real parts are less than zero the fixed point is stable, while if either is greater than zero the fixed point is unstable. If the factor inside the square root in equation 6.51 is positive, both eigenvalues are real, and the behavior near the fixed point will be exponential. This means that there will either be exponential movement toward the fixed point (if both eigenvalues are negative) or away from the fixed point if either eigenvalue is positive. We focus on the case when the factor inside the square root is negative, so that the square root is imaginary and the eigenvalues form a complex conjugate pair. In this case, the behavior near the fixed point is oscillatory and the trajectory will either spiral into the fixed point, if the real part of the eigenvalues is negative, or outward from the fixed point if the real part of the eigenvalues is positive. The imaginary part of the eigenvalue determines the frequency of oscillations near the fixed point. The real and imaginary parts of one of these eigenvalues are plotted as a function of τ_{I} in figure 6.15B. This figure indicates that the fixed point is stable if $\tau_{\mathrm{I}} < 40$ ms and unstable for larger values of τ_{I}.

Figures 6.16 and 6.17 show examples in which the fixed point is stable and unstable, respectively. In figure 6.16A, the oscillations in r_{E} and r_{I} are damped, and the firing rates settle down to the stable fixed point val-

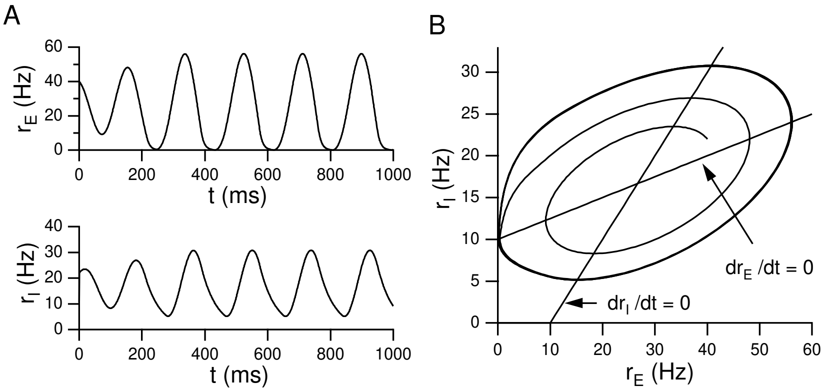

Figure 6.17: Activity of the excitatory-inhibitory firing-rate model when the fixed point is unstable. A) The excitatory and inhibitory firing rates settle into periodic oscillations. B) The phase-plane trajectory is a counter-clockwise spiral that joins the limit cycle, which is the closed orbit. For this example, $\tau_I = 50$ ms and all other parameters are as given in the text.

ues. The corresponding phase-plane trajectory is a collapsing spiral (figure 6.16B). In figure 6.17A the oscillations grow, and in figure 6.17B the trajectory is a spiral that expands outward until the system enters a limit cycle. A limit cycle is a closed orbit in the phase plane indicating periodic behavior. The fixed point is thus unstable in this case, and the limit cycle is stable. The transition from a fixed point to limit cycle behavior as a parameter is changed (in this case τ_I) making the real part of a complex eigenvalue change sign is called a Hopf bifurcation. This is one of the ways that a nonlinear system can make a transition from a stable fixed point to a limit cycle. In a Hopf bifurcation, the limit cycle emerges at a finite frequency, which is similar to the behavior of a type II neuron when it starts firing action potentials. Other types of bifurcations produce type I behavior with oscillations emerging at zero frequency. One example of this is a saddle node bifurcation, which occurs when two fixed points, one stable and one unstable, meet at the same point in phase space.

Firing-rate models greatly simplify neuronal dynamics, but they cannot account for temporal details of neuronal spiking beyond those described by a firing rate. Nevertheless, these models provide a compact description of at least some aspects of neuronal activity, and they are used extensively in studies of large neural networks. We will consider computational properties of firing-rate models in considerably more detail in chapter 7.

6.5 Appendices

A) Integrating the Membrane Potential

We begin by considering the integration of equation 6.22. It is convenient to rewrite this equation in the form

$$\tau_V \frac{dV}{dt} = V_\infty - V \, . \tag{6.52}$$

where $\tau_V = \tau_m$ and $V_\infty = E_\mathrm{L} + R_\mathrm{m} I_\mathrm{e}$. When the external current I_e is independent of time, the solution of this equation is

$$V(t) = V_\infty + (V(t_0) - V_\infty) \exp(-(t - t_0)/\tau_V) \tag{6.53}$$

where t_0 is any time prior to t and $V(t_0)$ is the value of V at time t_0. Equation 6.23 is a special case of this result with $t_0 = 0$.

If I_e depends on time, the solution 6.53 is not valid. An analytic solution can still be written down in this case (see exercise xx), but it is not particularly useful except in special cases. Over a small enough time period Δt, we can approximate $I_\mathrm{e}(t)$ as a constant and use the solution 6.53 to step from a time t to $t + \Delta t$. This requires replacing the variable t_0 in equation 6.53 with t and t with $t + \Delta t$ so that

$$V(t + \Delta t) = V_\infty + (V(t) - V_\infty) \exp(-\Delta t/\tau_V) \, . \tag{6.54}$$

This equation provides an updating rule for the numerical integration of equation 6.52. Provided that Δt is sufficiently small, repeated application of the update rule 6.54 provides an accurate way of determining the membrane potential. Furthermore, this method is stable because, if Δt is too large, it will only move V toward V_∞ and not, for example, make it grow without bound.

The equation for a general single-compartment conductance-based model, equation 6.1 with 6.2, can be written in the same form as equation 6.52 with

$$V_\infty = \frac{\sum_i \overline{g}_i m_i^{p_i} h_i^{q_i} E_i + I_\mathrm{e}/A}{\sum_i \overline{g}_i m_i^{p_i} h_i^{q_i}} \tag{6.55}$$

and

$$\tau_V = \frac{c_\mathrm{m}}{\sum_i \overline{g}_i m_i^{p_i} h_i^{q_i}} \, . \tag{6.56}$$

Note that if c_m is in units of nF/mm^2 and the maximal conductances in μS/mm^2, τ_V comes out in ms units. Similarly, if the reversal potentials are given in units of mV, I_e is in nA, and A is in mm^2, V_∞ will be in mV units.

If we take the time interval Δt to be small enough so that the gating variables can be approximated as constant during this period, the membrane potential can again be integrated over one time step using equation 6.54. Of course, the gating variables are not fixed, so once V has been updated by this rule, the gating variables must be updated as well.

B) Integrating the Gating Variables

All the gating variables in a conductance-based model satisfy equations of the same form,

$$\tau_z \frac{dz}{dt} = z_\infty - z \tag{6.57}$$

where we use z to denote a generic variable. Note that this equation has the same form as equation 6.52, and it can be integrated in exactly the same way. We assume that Δt is sufficiently small that V does not change appreciably over this time interval (and similarly [$\mathtt{Ca}^{2+}$] is approximated as constant over this interval if any of the conductances are $\mathtt{Ca}^{2+}$-dependent). Then, τ_z and z_∞, which are functions of V (and possibly [$\mathtt{Ca}^{2+}$]) can be treated as constants over this period and z can be updated by a rule identical to 6.54,

$$z(t + \Delta t) = z_\infty + (z(t) - z_\infty)\exp(-\Delta t/\tau_z). \tag{6.58}$$

An efficient integration scheme for conductance-based models is to alternate using rule (6.54) to update the membrane potential and rule (6.58) to update all the gating variables. It is important to alternate the updating of V with that of the gating variables, rather than doing them all simultaneously, as this keeps the method accurate to second order in Δt. If $\mathtt{Ca}^{2+}$-dependent conductances are included, the intracellular $\mathtt{Ca}^{2+}$ concentration should be computed simultaneously with the membrane potential.

C) Integrating Multi-Compartment Models

To solve the compartmental equations numerically, we must integrate one set of equations for each compartment. The gating variables can be handled as in the single compartment case using equation (6.58). Integrating the membrane potentials for the different compartments is more complex because they are coupled to each other.

The equation for the membrane potential within compartment μ, equation 6.31, can be written in the form

$$\frac{dV_\mu}{dt} = A_\mu V_{\mu-1} + B_\mu V_\mu + C_\mu V_{\mu+1} + D_\mu \tag{6.59}$$

where $A_\mu = c_m^{-1} g_{\mu,\mu-1}$, $B_\mu = -c_m^{-1}(\sum_i g_i^\mu + g_{\mu,\mu+1} + g_{\mu,\mu-1})$, $C_\mu = c_m^{-1} g_{\mu,\mu+1}$, and $D_\mu = c_m^{-1}(\sum_i g_i^\mu E_i + I_e^\mu/A_\mu)$. Note that the gating variables and other parameters have been absorbed into the values of A_μ, B_μ, C_μ, and D_μ in this equation. Equation 6.59, with μ running over all of the compartments of the model, generates a set of coupled differential equations. Because of the coupling between compartments, we cannot use the rule 6.54 to integrate these equations. Instead, we present another method that shares some of the positive features of rule 6.54.

Two of the most important features of an integration method are accuracy and stability. Accuracy refers to how closely numerical finite-difference methods reproduce the exact solution of a differential equation as a function of the integration step size Δt. Stability refers to what happens when Δt is chosen to be excessively large and the method starts to become inaccurate. A stable integration method will degrade smoothly as Δt is increased, producing results of steadily decreasing accuracy. An unstable method, on the other hand, will, at some point, display a sudden transition and generate wildly inaccurate results. For the present purposes, we want a method that is stable, even if this costs us somewhat in accuracy.

Defining

$$V_\mu(t + \Delta t) = V_\mu(t) + \Delta V_\mu \,, \tag{6.60}$$

the finite difference form of equation 6.59 gives the update rule

$$\Delta V_\mu = \left(A_\mu V_{\mu-1}(t) + B_\mu V_\mu(t) + C_\mu V_{\mu+1}(t) + D_\mu\right) \Delta t \tag{6.61}$$

which is how ΔV_μ is computed using the so-called Euler method. This method is both inaccurate and unstable. The stability of the method can be improved dramatically by evaluating the membrane potentials on the right side of equation 6.61 not at time t, but at a later time $t + \rho\Delta t$, so that

$$\Delta V_\mu = [A_\mu V_{\mu-1}(t + \rho\Delta t) + B_\mu V_\mu(t + \rho\Delta t) + C_\mu V_{\mu+1}(t + \rho\Delta t) + D_\mu]\Delta t \,. \tag{6.62}$$

Two such methods are predominantly used, the reverse Euler method for which $\rho = 1$ and the Crank-Nicholson method with $\rho = 0.5$. The reverse Euler method is the more stable of the two and the Crank-Nicholson is the more accurate. In either case, ΔV_μ is determined from equation 6.62. These methods are called implicit because equation 6.62 must be solved to determine ΔV_μ. To do this, we write $V_\mu(t + \rho\Delta t) \approx V_\mu(t) + \rho\Delta V_\mu$ and likewise for $V_{\mu\pm1}$. Substituting this into equation 6.62 gives

$$\Delta V_\mu = a_\mu \Delta V_{\mu-1} + b_\mu \Delta V_\mu + c_\mu \Delta V_{\mu+1} + d_\mu \tag{6.63}$$

where $a_\mu = A_\mu \rho\Delta t$, $b_\mu = B_\mu \rho\Delta t$, $c_\mu = C_\mu \rho\Delta t$ and $d_\mu = [D_\mu + A_\mu V_{\mu-1}(t) + B_\mu V_\mu(t) + C_\mu V_{\mu+1}(t)]\Delta t$.

Equation 6.63 for all μ values provides a set of coupled linear equations for the needed quantities ΔV_μ. An efficient method exists for solving these equations (Hines 1984, Tuckwell 1988). We illustrate the method for a single, unbranched cable and leave the extension to a branched cable as an exercise for the reader (exercise xx). The cable we consider begins with the compartment $a = 1$, so $a_1 = 0$ and it ends at compartment N, so $c_N = 0$. The method consists of solving (6.63) for ΔV_μ in terms of $\Delta V_{\mu+1}$ sequentially starting at one end of the cable and proceeding to the other end. For example, if we start the procedure at compartment one, ΔV_1 can be expressed as

$$\Delta V_1 = \frac{c_1 \Delta V_2 + d_1}{1 - b_1} \,. \tag{6.64}$$

Substituting this into the equation (6.63) for ΔV_2 gives

$$\Delta V_2 = \tilde{b}_2 \Delta V_2 + c_2 \Delta V_3 + \tilde{d}_2 \tag{6.65}$$

where $\tilde{b}_2 = b_2 + a_2 c_1/(1 - b_1)$ and $\tilde{d}_2 = d_2 + a_2 d_1/(1 - b_1)$. We now repeat the procedure going down the cable. At each stage, we solve for $\Delta V_{\mu-1}$ in terms of ΔV_μ finding

$$\Delta V_{\mu-1} = \frac{c_{\mu-1} \Delta V_\mu + \tilde{d}_{\mu-1}}{1 - \tilde{b}_{\mu-1}}. \tag{6.66}$$

and define

$$\tilde{b}_{\mu+1} = b_{\mu+1} + \frac{a_{\mu+1} c_\mu}{1 - \tilde{b}_\mu} \tag{6.67}$$

and

$$\tilde{d}_{\mu+1} = d_{\mu+1} + \frac{a_{\mu+1} \tilde{d}_\mu}{1 - \tilde{b}_\mu}. \tag{6.68}$$

Finally, when we get to the end of the cable we can solve for

$$\Delta V_N = \frac{\tilde{d}_N}{1 - \tilde{b}_N} \tag{6.69}$$

because $c_N = 0$.

The procedure for finding the ΔV_μ is the following. Define $\tilde{b_1} = b_1$ and $\tilde{d_1} = d_1$ and iterate equations 6.67 and 6.68 down the length of the cable to define all the $\tilde{b}$'s and $\tilde{d}$'s. Then, solve for ΔV_N from equation 6.69 and iterate back up the cable solving for the ΔV's using 6.66. This process takes only $2N$ steps. As the reader can show in exercise xx, a similar procedure can be used for a branching cable. The equations are solved starting at the ends of both branches and moving in toward the branching node, then continuing on as for an unbranched cable, and finally reversing direction and completing the solution moving in the opposite direction along the cable and i ts branches.

6.6 Further Reading and References

Further Reading

Hodgkin, AL & Huxley, AF (1952) A quantitative description of membrane current and its application to conduction and excitation in nerve. *Journal of Physiology (London)* **117**:500-544.

Johnston, D & Wu, SM (1995) *Foundations of Cellular Neurophysiology*. Cambridge, MA:MIT Press.

Koch, C (1998) *Biophysics of Computation: Information Processing in Single Neurons*. New York:Oxford University Press.

Koch, C & Segev, I, editors (1998) *Methods in Neuronal Modeling: From Synapses to Networks*. Cambridge, MA:MIT Press.

McCormick, DA (1990) Membrane properties and neurotransmitter actions. In GM Shepherd, editor, *The Synaptic Organization of the Brain*. New York:Oxford University Press.

Tuckwell, HC (1988) *Introduction to Theoretical Neurobiology*. Cambridge, UK:Cambridge University Press.

References

Bell, A (1992) Self-Organization in real neurons: anti-Hebb in 'channel space'? In JE Moody and SJ Hanson, editors, *Neural Information Processing Systems 4*. San Mateo CA:Morgan Kaufman, pp. 59-66.

Bressloff, PC & Coombes, S (1999) Dynamics of strongly coupled spiking neurons. Submitted to *Neural Computation.*

Bugmann, G, Christodoulou, C & Taylor, JG (1997) Role of temporal integration and fluctuation detection in the highly irregular firing of a leaky integrator neuron model with partial reset. *Neural Computation* **9**:985-1000.

Connor, JA & Stevens CF (1971) Prediction of repetitive firing behavior from voltage clamp data on an isolated neuron soma. *Journal of Physiology* **213**:31-54.

Connor, JA, Walter, D & McKown, R (1977) Neural repetitive firing: modifications of the hodgkin-Huxley axon suggested by experimental results from crustacean axons. *Biophysical Journal* **18**:81-102.

Ermentrout, B (1998) Neural networks as spatio-temporal pattern-forming systems. *Reports on Progress in Physics* **64**:353-430.

FitzHugh, R (1961) Impulses and physiological states in models of nerve membrane. *Biophysical Journal* **1**:445-466.

Freeman, WJ & Schneider, W (1982) Changes in spatial patterns of rabbit olfactory EEG with conditioning to odors. *Psychophysiology* **19**:44-56.

Gerstner, W (1998) Spiking neurons. In W Maass & CM Bishop, editors, *Pulsed Neural Networks* Cambridge, MA: MIT press: 3-54.

Haberly, LB (1990) Olfactory cortex. In GM Shepherd, editor, *The Synaptic Organization of the Brain*. New York:Oxford University Press.

Hines, M (1984) Efficient computation of brancehd nerve equations. *International Journal of Biomedical Computation* **15**:69-76.

Huguenard, JR & McCormick, DA (1992) Simulation of the currents involved in rhythmic oscillations in thalamic relay neurons. *Journal of Neurophysiology* **68**:1373-1383.

LeMasson, G, Marder, E & Abbott, LF (1993) Activity-Dependent Regulation of Conductances in Model Neurons. *Science* **259**:1915-1917.

Li, Z (1995). Modeling the sensory computations of the olfactory bulb. In JL van Hemmen, E Domany & K Schulten, editors, *Models of Neural Networks, Volume 2.* New York: Springer Verlag.

Li, Z (1990) A model of olfactory adaptation and sensitivity enhancement in the olfactory bulb. *Biological Cybernetics* **62**:349-361.

Li, Z & Hopfield, J (1989) Modeling the olfactory bulb and its neural oscillatory processings. *Biological Cybernetics* **61**:379-392.

Morris, C & Lecar, H (1981) Voltage oscillations in the barnacle giant muscle fiber. *Biophysical Journal* **35**:193-213.

Nagumo, JS, Arimoto, S & Yoshizawa, S (1962) *Proceedings of the IRE* **50**:2061-2074.

Shadlen, MN & Newsome, WT (1994) Noise, neural codes and cortical organization. *Current Opinion in Neurobiology* **4**:569-579.

Softky, WR & Koch, C (1992) Cortical cells should spike regularly but do not. *Neural Computation* **4**:643-646.

Softky, WR & Koch, C (1994) The highly irregular firing of cortical cells is inconsistent with temporal integration of random EPSPs. *Journal of Neuroscience* **13**:334-350.

Stemmler, M & Koch, C (1999) Information maximization in single neurons. (unpublished).

Troyer, TW & Miller, KD (1997) Physiological gain leads to high ISI variability in a simple model of a cortical regular spiking cell. *Neural Computation* **9**:971-983.

Van Vreeswijk, C, Abbott, LF & Ermentrout, GB (1994) When Inhibition Not Excitation Synchronizes Neuronal Firing. *Journal of Computational Neuroscience* **1**:313-321.

Wang, X.-J. (1994) Multiple dynamical modes of thalamic relay neurons: Rhythmic bursting and intermittent phase-locking. *Neuroscience* **59**:21-31.

Wang, X.-J. & Rinzel, J (1992) Alternating and synchronous rhythms in reciprocally inhibitory model neurons. *Neural Computation* **4**:84-97.

Turrigiano, G, LeMasson, G & Marder, E (1995) Selective regulation of current densities underlies spontaneous changes in the activity of cultured neurons. *Journal of Neuroscience* **15**:3640-3652.

Wilson, HR & Cowan, JD (1972) Excitatory and inhibitory interactions in localized populations of model neurons. *Biophysical Journal* **12**:1-24.

6.7 Exercises

1. Show that the Hodgkin-Huxley model produces a type II firing-rate curve in response to constant current injection.

2. Demonstrate postinhibitory rebound in the Hodgkin-Huxley model.

3. Construct a Morris-Lecar model neuron (Morris and Lecar, 1981). This is probably the simplest conductance-based model with interesting dynamics. Instead of modeling the fast sodium spikes of an action potential, it models slower calcium spikes that can produce bursting behavior in neurons. The model has just two active currents, an instantaneous voltage-dependent $\mathtt{Ca}^{2+}$ current and a persistent potassium current, described by a single dynamical gating variable n,

$$i_{\mathrm{m}} = \overline{g}_L(V - E_{\mathrm{L}}) + \overline{g}_{Ca} m_\infty(V)(V - E_{Ca}) + \overline{g}_K n(V - E_{\mathrm{K}}) \quad (6.70)$$

with $\overline{g}_L$ = 0.5 mS/cm^2, $\overline{g}_{Ca}$ = 1 mS/cm^2 and $\overline{g}_K$ = 2 mS/cm^2, E_{L} = -50 mV, E_{Ca} = 100 mV and E_{K} = -70 mV. The function m_∞ is given by

$$m_\infty = \frac{1}{1 + \exp[-.133(V + 1)]} \quad (6.71)$$

and the gating variable n is given by

$$\tau_n \frac{dn}{dt} = n_\infty - n \quad (6.72)$$

with

$$\tau_n = \frac{3}{\cosh[.0345(V - 10)]} \qquad n_\infty = \frac{1}{1 + \exp[-.138(V - 10)]} \quad (6.73)$$

Determine the firing rate as a function of injected current and plot the membrane potential both as a function of time and in a phase-plane trajectory along with the n variable. In the phase plane, plot the nullclines for the V and n equations.

4. Construct a reciprocal two-neuron oscillator model (due to F. Skinner and E. Marder). For both cells, the membrane current is

$$i_{\mathrm{m}} = \overline{g}_L(V - E_{\mathrm{L}}) + \overline{g}_H z(V - E_H) \quad (6.74)$$

where $\overline{g}_L$ = 0.0111 mS/cm^2, $\overline{g}_H$ = 0.5 mS/cm^2, E_{L} = -60 mV, and E_H = -10 mV. The H-current is a hyperpolarization activated current determined by

$$\tau_z(V)\frac{dz}{dt} = z_\infty(V) - z \quad (6.75)$$

with

$$r_\infty(V) = \frac{1}{1 + \exp\left[(V + 50)/7\right]} \quad \text{and} \quad \tau_r(V) = \frac{3030.3}{1 + \exp\left[(-V - 110)/13\right]} . \quad (6.76)$$

The synaptic connection between these neurons is modeled as a graded function of the presynaptic membrane potential. The synaptic current for a postsynaptic neuron with membrane potential V_{post} is

$$I_{syn} = \overline{g}_s s(V_{post} - E_{\mathrm{s}}) \tag{6.77}$$

where E_{s} = -80 mV and $\overline{g}_s$ = 0.5 mS/cm^2. The variable s is determined by the membrane potential of the presynaptic neuron, V_{pre}, by

$$\tau_{\mathrm{s}}(1 - s_\infty(V_{pre}))\frac{ds}{dt} = s_\infty(V_{pre}) - s \tag{6.78}$$

with $\tau_{\mathrm{s}} = 50$ ms and

$$s_\infty(V_{pre}) = [\tanh((V_{pre} + 57)/10))]_+ \tag{6.79}$$

where $[z]_+ = z$ if $z \geq 0$ and $[z]_+ = 0$ if $z < 0$.

5. The FitzHugh-Nagumo equations (FitzHugh, 1961; Nagumo *et al*, 1962) are given by

$$\frac{dv}{dt} = v(1 - v^2) - u + I_{\mathrm{e}} \quad \text{and} \quad \frac{du}{dt} = \epsilon(v - 0.5u) \tag{6.80}$$

Draw the nullclines for these equations for $I_{\mathrm{e}} = 0$ and $I_{\mathrm{e}} = -1$. These are the lines in the x-y plane where the right sides of these two equations are zero. In which case or cases do you think the model will produce oscillations? Next simulate the model to see what happens when these equations are integrated over time. Determine what happens for $I_{\mathrm{e}} = 0$ with ϵ = 0.3, 0.1, and 1 and for $I_{\mathrm{e}} = -1$ with $\epsilon = 0.3$.

6. Write down the analytic solution of equation 6.52 when $I_{\mathrm{e}}(t)$ is an arbitrary function of time. The solution will involve integrals that cannot be performed unless $I_{\mathrm{e}}(t)$ is specified.

7. Construct the model of two, coupled integrate-and-fire model neurons of figure 6.10. Show how the pattern of firing for the two neurons depends on the strength, type (excitatory or inhibitory), and time constant of the reciprocal synaptic connection (see Van Vreeswijk *et al*, 1994).

8. Construct a non-branching axonal cable with conductances in each compartment described by the Connor-Stevens model. Plot the action potential propagation velocity as a function of the axon radius.

9. Simulate the dynamics of the firing-rate model of coupled excitatory and inhibitory neural populations given by equations 6.48 and 6.49. Choose a parameter range different from that discussed in the text, and compare the behavior of the model to what you expect on the basis of a fixed-point stability analysis.

10. Determine the numerical solution for a multi-compartment cable with a single branch node analogous to the solution for a non-branching cable given in appendix C.